

Prestellar Cores in Turbulent Clouds: Properties of Critical Cores

SANGHYUK MOON¹ AND EVE C. OSTRIKER¹¹*Department of Astrophysical Sciences, Princeton University, Princeton, NJ 08544, USA*

ABSTRACT

A fraction of the dense cores within a turbulent molecular cloud will eventually collapse to form stars. Identifying the physical criteria for instability and analyzing critical core properties is therefore necessary to star formation theory. Here we quantify the characteristics of an ensemble of “critical cores” on the verge of collapse. This critical epoch was identified in a companion paper, which followed the dynamical evolution of prestellar cores in numerical simulations of turbulent, self-gravitating clouds. We find that radial profiles of density and turbulent velocity dispersion in individual critical cores are consistent with our new model for turbulent equilibrium spheres (TESs). While a global linewidth–size relation exists for a cloud with given size and Mach number, the turbulent scaling relations around each core exhibit significant variations. As a result, there is no single density threshold for collapse; instead, cores collapse at a range of densities determined by the local sonic scale and gravitational potential environment. The critical cores in our simulations are mostly transonic; we do not find either purely thermal or highly turbulent cores. In our low Mach number model which better resolves the characteristic mass and sonic scales, we find marginal evidence that the core mass function (CMF) of critical cores peaks around a characteristic mass scale associated with the large-scale cloud properties. We highlight the importance of constructing the CMF at the critical time for the purpose of testing gravoturbulent fragmentation theories, and derive the resolution requirements to unambiguously identify the peak of the CMF.

1. INTRODUCTION

Dense cores are transient structures within turbulent giant molecular clouds (GMCs), with their properties continuously changing in space and time (see Bergin & Tafalla 2007; di Francesco et al. 2007; McKee & Ostriker 2007; André et al. 2014; Offner et al. 2014; Padoan et al. 2014, for related reviews). While the physical properties of *prestellar* cores — which ultimately collapse, leading to star formation — are of great interest, it has not been clear exactly what the criterion is for a given core to become unstable and therefore unambiguously “prestellar.” In observational surveys, the simplest working definition for prestellar candidates is cores that appear gravitationally bound, based on estimates of their internal energy, although more detailed criteria have also been applied (e.g. Andre et al. 2000; Könyves et al. 2015). However, simulations that trace the evolution of dense structures show that many stochastically cycle through different phases (due to their turbulent environment), rather than following a single evolutionary sequence, and in particular cores with “prestellar”

characteristics sometimes subsequently disperse (Offner et al. 2022).

Notwithstanding the ambiguities in recognizing prestellar cores, their very nature — objects that will collapse to form a star or stellar system in the near future — provides at least two physically meaningful common reference points in time shared across all cores: (1) The time when they *initiate* gravitational runaway (hereafter “critical time”) and (2) the instant they *complete* it by forming a nascent protostar at the center (“collapse time”). While these milestones would be essentially impossible to pinpoint in observations, they can be identified on an individual core basis within numerical simulations of gravo-turbulent fragmentation.

The second of the two above events is easier to pick out in simulations, since this is when runaway collapse leads to a $\rho \propto r^{-2}$ singular density profile (Larson 1969; Penston 1969).¹ In particular, in numerical simulations where collapsing centers are replaced with sink particles, the collapse time of each core can be identified as the moment when a sink particle is created. For exam-

sanghyuk.moon@princeton.edu, eco@astro.princeton.edu

¹ Strictly speaking, it is only at the center of this power-law profile that a protostar-disk system begins to grow.

ple, Gong & Ostriker (2015), Padoan et al. (2020), and Pelkonen et al. (2021) used the closest snapshot to the creation time of each sink particle to define their “progenitor core” as a gravitationally bound region around the site where the sink is created.

By measuring the core mass at each core’s collapse time, Gong & Ostriker (2015) demonstrated that the core mass function (CMF) has a well-defined peak which converges with increasing numerical resolution. Pelkonen et al. (2021), taking a slightly different approach, varied the resolution for the clumpfind algorithm rather than the underlying simulation resolution, and also found convergence in the CMF at the time of collapse. In the majority of numerical studies of gravo-turbulent fragmentation, however, it is not the CMF at a characteristic epoch for each core or sink’s evolution that is measured, but instead the sink particle mass function (SMF) at an arbitrarily selected time common to all particles (e.g., Haugbølle et al. 2018; Lee & Hennebelle 2018; Guszejnov et al. 2020). The resulting SMF has not shown numerically converging behavior, unlike the CMF based on individual collapse times (see, however, Haugbølle et al. 2018; Pelkonen et al. 2021). As we shall discuss, the reason for the difference between CMF convergence and SMF non-convergence likely relates to fragmentation in late stages of evolution. But in any case, in order to test theories of turbulent fragmentation that are the basis for models of the initial mass function (e.g., Padoan & Nordlund 2002; Hennebelle & Chabrier 2008; Hopkins 2012), it is necessary to construct the CMF itself at characteristic epochs of evolution.

While the collapse time provides a convenient reference point and can be easily identified in numerical simulations, it is the *critical time* that is most relevant for the point of comparison to theories. Collins et al. (2024), by analyzing the collapse histories of simulated cores via tracer particles, found that there exists a characteristic epoch after which mass is rapidly delivered to the core center, raising the core density in a runaway fashion. Based on this observation they defined a proxy for the critical time (termed “singularity time” in their work) by choosing a threshold on the density time derivative. They found that, as each core approaches its critical time, the radial density profiles of cores develop a characteristic core–envelope structure while the mean radial and tangential velocities exhibit a common behavior of increasing in magnitude with increasing radius. The identification of this characteristic epoch reveals a common physical process occurring in an ensemble of cores that is otherwise blurred by evolution. However, the question of what determines this critical time still remains to be answered.

Related to the critical time is a common narrative for the evolution of prestellar cores, where certain critical conditions trigger gravitational runaway (McKee & Ostriker 2007; André et al. 2014; Offner et al. 2014; Padoan et al. 2014). Among others, the Bonnor-Ebert (BE) sphere and its stability property (Ebert 1955; Bonnor 1956; Ebert 1957) have often been used as a theoretical tool for determining critical conditions (e.g., Krumholz & McKee 2005; Padoan & Nordlund 2011). However, the applicability of the BE model to cores within turbulent molecular clouds is limited, because (1) real cores exist as a part of a turbulent continuum unlike an isolated BE sphere truncated by “external pressure,” and (2) the model does not account for internal turbulent velocities expected for cores forming within a turbulent cloud.

In a series of papers, we have begun a comprehensive analysis of prestellar core evolution to address the limitations pertaining to the BE model and to answer the question of exactly what triggers the onset of collapse. In Moon & Ostriker (2024a, hereafter *Paper I*), we developed a new theoretical model for equilibrium spherically-symmetric cores supported by both thermal and turbulent pressure, with the solutions obtained by directly solving the time-steady, angle-averaged equations of hydrodynamics. A distinguishing feature of the resulting family of solutions, which we term the turbulent equilibrium sphere (TES), is that the turbulent pressure naturally arises from a power-law velocity structure function rather than from a phenomenological equation of state. The TES model also enjoys a useful behavior of reducing to the BE model in the limit of vanishing turbulent velocities. *Paper I* found that, similar to the case for BE spheres, solutions can be classified as stable or unstable to radial perturbations. For a given set of turbulence parameters and central density, cores exceeding a certain critical size are unstable. The radius, mass, and center-to-edge density contrast of critical TESs all increase with increasing turbulent velocity dispersion (or equivalently, decreasing sonic scale). This implies that a nascent core forming in a highly turbulent region would initially be in the stable, subcritical regime.

Based on the stability properties of TESs and from a general consideration of tidal gravitational fields in core-forming regions, *Paper I* proposed an evolutionary scenario for “successful” prestellar cores formed by converging turbulent flows. In this scenario, nascent cores evolve in the direction of increasing density (as mass is added) and decreasing turbulence (as dissipation progresses). When converging flows are strong enough or turbulence sufficiently dissipates, the critical radius r_{crit}

moves inside the “tidal radius” r_{tidal} set by the landscape of the gravitational potential, and a core becomes unstable and collapses. Otherwise, it remains stable and is eventually dispersed by turbulence (see Figure 11 of Paper I for a schematic illustration for this scenario). To test this scenario and identify the critical conditions for collapse, in Moon & Ostriker (2024b) (hereafter Paper II) we conducted and carefully analyzed a suite of numerical simulations of turbulent, self-gravitating clouds. Paper II presents results from a comprehensive analysis of each core’s dynamical evolution from its formation, through the onset of collapse, to the point when the central density blows up, signaling the beginning of the protostellar phase. By measuring radial forces acting within the cores over time, Paper II directly identified the critical time when the net radial force becomes negative, instigating runaway collapse. We found good agreement between the empirically identified critical time and the epoch when a core is predicted to be unstable according to the TES model, thus providing an answer as to what determines the critical time.

In this paper, we analyze the simulation results of Paper II at the critical time of each core to investigate the physical properties of prestellar cores at the onset of collapse. We shall show that the cores defined at their respective critical time (referred to as “critical cores” throughout this work) are mostly transonic in terms of their internal turbulence (turbulent Mach number ~ 0.5 – 1.5), with their structure overall consistent with the TES model. We shall also show that the local turbulent scaling relations within each core exhibit significant variations above and below the average linewidth–size relation for the entire cloud, with higher density in more turbulent critical cores. As a result, there is a wide range of critical densities for collapse, rather than a single threshold density. We shall also present statistical distributions of core masses, sizes, densities, durations of different evolutionary stages, and accretion rates.

The remainder of this paper is organized as follows. In Section 2, we define key physical quantities related to our TES model and numerical simulations. In Section 3, we first (Section 3.1) present the radial density and velocity dispersion profiles of critical cores and compare them with the TES models. We then (Section 3.2) show that the locally constructed linewidth–size relations exhibit significant variations around the mean relation, causing cores to become unstable at a wide range of densities (Section 3.3). We also present probability distributions of various physical quantities measured for critical cores, including the CMF (Section 3.4). Section 4 presents the evolution of the mass inflow rates and, by using them, characterizes evolution-

ary timescales at each stage. We discuss implications of our results in Section 5 and conclude in Section 6.

2. KEY DEFINITIONS

In this section, we provide key concepts and definitions of physical quantities that will be used throughout the paper. We refer the reader to Paper I and Paper II for complete descriptions of our TES model and numerical simulations, respectively.

2.1. TES Model

The radius and mass scales most relevant to isothermal self-gravitating objects supported entirely by thermal pressure are the critical BE radius and mass given by

$$R_{\text{BE}}(\bar{\rho}) = 0.762 \frac{c_s}{G^{1/2} \bar{\rho}^{1/2}}, \quad (1)$$

$$M_{\text{BE}}(\bar{\rho}) \equiv \frac{4\pi}{3} \bar{\rho} R_{\text{BE}}^3(\bar{\rho}) = 1.86 \frac{c_s^3}{G^{3/2} \bar{\rho}^{1/2}}, \quad (2)$$

where $c_s = (kT/\mu)^{1/2}$ is the isothermal sound speed with temperature T and mean molecular weight μ , G is the gravitational constant, and $\bar{\rho}$ is the average density within a core.

Paper I generalized these results for TESs characterized by the power-law linewidth–size relation of the form

$$\langle \delta v_r^2 \rangle_\rho^{1/2} = c_s \left(\frac{r}{r_s} \right)^p = c_s \left(\frac{\xi}{\xi_s} \right)^p, \quad (3)$$

where $\delta v_r \equiv v_r - \langle v_r \rangle_\rho$ is the radial velocity fluctuation (meridional, δv_θ , and azimuthal, δv_ϕ , velocity fluctuations are similarly defined), r_s is the sonic radius, and p is the power-law index. In the second equality,

$$\xi \equiv \frac{\sqrt{4\pi G \rho_c} r}{c_s} \quad (4)$$

is the dimensionless radius normalized with respect to the central density ρ_c , which also defines the dimensionless sonic radius ξ_s where $r = r_s$. The angled bracket in Equation (3) is a mass-weighted angle-averaging operator defined by

$$\langle Q \rangle_\rho \equiv \frac{\oint_{4\pi} \rho Q d\Omega}{\oint_{4\pi} \rho d\Omega}, \quad (5)$$

where ρ is gas density and Q is a physical quantity to be averaged. It is related to the volume-weighted average

$$\langle Q \rangle \equiv \frac{1}{4\pi} \oint_{4\pi} Q d\Omega \quad (6)$$

by $\langle Q \rangle_\rho \equiv \langle \rho Q \rangle / \langle \rho \rangle$.

Under a given turbulent velocity field defined by Equation (3), there exists a family of quasi-equilibrium TES

solutions parametrized by ξ_s and p . These solutions are unstable when their maximum radial extent in terms of dimensionless ξ exceeds the critical value ξ_{crit} . For a given central density ρ_c , the critical radius in physical units is given by

$$r_{\text{crit}}(\rho_c) = \frac{\xi_{\text{crit}}}{(4\pi)^{1/2}} \frac{c_s}{G^{1/2} \rho_c^{1/2}}, \quad (7)$$

where the corresponding mass within r_{crit} defines the critical mass

$$M_{\text{crit}}(\rho_c) = \frac{m_{\text{crit}}}{(4\pi)^{1/2}} \frac{c_s^3}{G^{3/2} \rho_c^{1/2}}. \quad (8)$$

Here, ξ_{crit} and m_{crit} are the dimensionless critical radius and critical mass, respectively, for which [Paper I](#) provides solutions as functions of p and ξ_s (see Figure 4 of [Paper I](#); see also Equations (56)–(57) of [Paper I](#) for alternative expressions of r_{crit} and M_{crit} based on the edge and average densities). Both ξ_{crit} and m_{crit} decrease with increasing ξ_s , approaching the well-known BE limit $\xi_{\text{crit}} = 6.45$ and $m_{\text{BE}} = 15.7$ as $\xi_s \rightarrow \infty$.

For $p = 0.5$, [Paper I](#) found approximate relations to characterize how turbulence enhances the critical radius and mass for given mean density $\bar{\rho} \equiv 3M_{\text{crit}}/(4\pi r_{\text{crit}}^3) = 3\rho_c m_{\text{crit}}/\xi_{\text{crit}}^3$:

$$r_{\text{crit}}(\bar{\rho}) \approx R_{\text{BE}}(\bar{\rho}) \left(1 + \frac{1}{2} \frac{\sigma_{1\text{D}}^2}{c_s^2}\right)^{1/3}, \quad (9)$$

$$M_{\text{crit}}(\bar{\rho}) \approx M_{\text{BE}}(\bar{\rho}) \left(1 + \frac{1}{2} \frac{\sigma_{1\text{D}}^2}{c_s^2}\right), \quad (10)$$

which are valid within relative error of 5% for $\sigma_{1\text{D}}/c_s < 9.5$ and $\sigma_{1\text{D}}/c_s < 13$, respectively, and where

$$\sigma_{1\text{D}} \equiv \frac{1}{\sqrt{3}} \left(\frac{\int \rho |\mathbf{v} - \mathbf{v}_{\text{com}}|^2 d\mathcal{V}}{\int \rho d\mathcal{V}} \right)^{1/2} \quad (11)$$

is the mass-weighted one-dimensional velocity dispersion relative to the center of mass velocity $\mathbf{v}_{\text{com}} \equiv (\int \rho \mathbf{v} d\mathcal{V})/(\int \rho d\mathcal{V})$. The volume integral is performed over a ball of radius r_{crit} in the context of the TES model and our simulated cores. While in general, ordered motions such as inflow, outflow, or rotation, can contribute to $\sigma_{1\text{D}}$ in addition to random turbulent motions, such bulk components are assumed to be zero in the TES model and found to be subdominant for our simulated cores except near the end of the collapse (see Appendix B of [Paper II](#).) An important point to note is that [Equations \(9\) and \(10\)](#) do not simply substitute $c_s^2 \rightarrow c_s^2 + \sigma_{1\text{D}}^2$ in [Equations \(1\) and \(2\)](#), but rather,

there are different functional dependences on turbulent and thermal velocities.²

We note that from the definitions in [Equation \(3\)](#) and [Equation \(11\)](#), the internal velocity dispersion, core radius, and sonic radius at the critical time are related by (see Appendix B of [Paper II](#) for details)

$$\frac{\sigma_{1\text{D}}}{c_s} = \eta_d \left(\frac{3}{2p+3} \right)^{1/2} \left(\frac{r_{\text{crit}}}{r_s} \right)^p, \quad (12)$$

where η_d is almost constant at $\eta_d \approx 0.9$, with very weak dependence on p and $\sigma_{1\text{D}}$. Thus, trans-sonic cores with $p \sim 1/3 - 1/2$ have $r_{\text{crit}}/r_s \sim 1$, and more generally $\sigma_{1\text{D}}/c_s \approx 0.8(r_{\text{crit}}/r_s)^p$.

For a given power law index p , the TES solutions show that critical cores have a dimensionless sonic radius ξ_s (see [Equation \(4\)](#) for definition) that monotonically decreases with increasing $\sigma_{1\text{D}}/c_s$ (see Figure 4(d) of [Paper I](#)). For $p = 0.5$, we find that an approximate relation

$$\xi_s \approx 2.42 + 4 \left(\frac{\sigma_{1\text{D}}}{c_s} \right)^{-2}, \quad (13)$$

holds within a relative error of 1.85% for $\sigma_{1\text{D}} < 10c_s$.

If a core with critical radius r_{crit} (based on its central density) and velocity dispersion $\sigma_{1\text{D}}$ is in a state of turbulent quasi-equilibrium, with a linewidth-size index $p = 0.5$, [Equations \(1\) and \(9\)](#) imply that its average density within r_{crit} would be approximately

$$\bar{\rho}_{\text{TES}} \equiv 0.581 \frac{c_s^2}{Gr_{\text{crit}}^2} \left(1 + \frac{1}{2} \frac{\sigma_{1\text{D}}^2}{c_s^2} \right)^{2/3}. \quad (14)$$

This can be regarded as a prediction of the TES theory relating the radius, mean density, and velocity dispersion of critical cores. As a generalization of the classical BE relation, the prediction in [Equation \(14\)](#) can be compared to both simulations (as we shall do in this paper) and to observations.

2.2. Hydrodynamic Calculations

The initial condition of the turbulent cloud simulations conducted in [Paper II](#) consists of uniform density ρ_0 in a periodic box of side length L_{box} , with turbulent velocity perturbations randomly initialized from a Gaussian distribution with a k^{-2} power spectrum (corresponding to a linewidth-size relation $\Delta v(l) \propto l^{1/2}$). The velocity dispersion averaged over the simulation box,

² For the high-turbulence regime $\sigma_{1\text{D}}/c_s \gtrsim 10$, a better fit replaces $0.5(\sigma_{1\text{D}}/c_s)^2$ in both relations by $0.16(\sigma_{1\text{D}}/c_s)^{2.5}$. However, this regime is not relevant to the critical cores found in our simulations.

$\sigma_{1D, \text{box}}$, is related to the specified three-dimensional Mach number by $\mathcal{M}_{3D} = \sqrt{3}\sigma_{1D, \text{box}}/c_s$.

In all our simulations, we adopt an isothermal equation of state with

$$c_s = 0.188 \text{ km s}^{-1} \left(\frac{T}{10 \text{ K}} \right)^{1/2}, \quad (15)$$

assuming $\mu = 2.3m_H$ appropriate for 10% helium abundance by number. Apart from the dependence on a random seed for initializing the turbulent velocity field, the initial conditions are fully specified with the two dimensionless parameters: the number of Jeans lengths initially contained in the domain, $L_{\text{box}}/L_{J,0}$, and the root-mean-square Mach number \mathcal{M}_{3D} averaged within the cubic volume L_{box}^3 . Here,

$$L_{J,0} \equiv \left(\frac{\pi c_s^2}{G \rho_0} \right)^{1/2} = 1.93 \text{ pc} \left(\frac{T}{10 \text{ K}} \right)^{1/2} \left(\frac{n_{H,0}}{200 \text{ cm}^{-3}} \right)^{-1/2} \quad (16)$$

is the Jeans length at the cloud's average density $\rho_0 = 1.4m_H n_{H,0}$. The corresponding mass and time scales are the Jeans mass

$$M_{J,0} \equiv \rho_0 L_{J,0}^3 = 49.9 M_\odot \left(\frac{T}{10 \text{ K}} \right)^{3/2} \left(\frac{n_{H,0}}{200 \text{ cm}^{-3}} \right)^{-1/2} \quad (17)$$

and the Jeans time

$$t_{J,0} \equiv \frac{L_{J,0}}{c_s} = 10.0 \text{ Myr} \left(\frac{n_{H,0}}{200 \text{ cm}^{-3}} \right)^{-1/2}, \quad (18)$$

which is related to the cloud's free-fall time

$$\begin{aligned} t_{\text{ff},0} &\equiv \left(\frac{3\pi}{32G\rho_0} \right)^{1/2} = 0.306 t_{J,0} \\ &= 3.08 \text{ Myr} \left(\frac{n_{H,0}}{200 \text{ cm}^{-3}} \right)^{-1/2}. \end{aligned} \quad (19)$$

In [Paper II](#), we presented results from 40 simulations conducted with $\mathcal{M}_{3D} = 5$ (model M5) and 7 simulations with $\mathcal{M}_{3D} = 10$ (model M10), varying the random seed for the initial cloud turbulence. The box sizes for model M5 and M10 are set to $L_{\text{box}} = 2L_{J,0}$ and $4L_{J,0}$, respectively, to fix the cloud-scale effective virial parameter at

$$\alpha_{\text{vir}, \text{box}} \equiv \frac{5\sigma_{1D, \text{box}}^2 L_{\text{box}}}{2GM_{\text{box}}} = 1.66, \quad (20)$$

where $M_{\text{box}} = L_{\text{box}}^3 \rho_0$ is the total mass in the computational domain. The chosen box size and Mach number set the average sonic radius,

$$r_{s, \text{cloud}} \equiv \frac{9}{8} \frac{L_{\text{box}}}{\mathcal{M}_{3D}^2} = 0.579 L_{J,0} \alpha_{\text{vir}, \text{box}}^{-1/2} \mathcal{M}_{3D}^{-1}, \quad (21)$$

at which turbulent velocity dispersion following the cloud's mean linewidth-size relation equals the sound

speed; the factor 9/8 accounts for the conversion between three-dimensional volume-average \mathcal{M}_{3D} and one-dimensional shell-average $\langle \delta v_r^2 \rangle_\rho^{1/2}$ (see Equations (14) and (16) in [Paper II](#)).

We choose physical and numerical parameters for our simulations by requiring both the overall sonic scale of the turbulence and the size of self-gravitating cores that subsequently form to be resolved. Cores that develop in simulations of turbulent clouds have densities comparable to the post-shock value at the global Mach number of the cloud, $\rho \sim \rho_{\text{ps}} = \mathcal{M}_{3D}^2 \rho_0$. [Equation \(21\)](#) thus indicates that, for realistic cloud models with $\alpha_{\text{vir}, \text{box}} \gtrsim 2$, resolving the sonic radius in ambient gas poses a similar challenge to resolving dense cores, which have typical sizes on the order of $R_{\text{BE}}(\rho_{\text{ps}}) = 0.430 L_{J,0} \mathcal{M}_{3D}^{-1}$. With the goal of having $r_{s, \text{cloud}}$ sufficiently resolved everywhere and also having cores resolved down to a mass $M_{\text{BE}}(2\rho_{\text{ps}})$ we adopt uniform resolution with the number of cells per dimension $N = 1024$ for model M10 and $N = 512$ for M5 (see Section 3.3 of [Paper II](#) for details on the resolution requirements). The resulting cell size normalized to the average Jeans length is $\Delta x/L_{J,0} = (L_{\text{box}}/N)/L_{J,0} = 3.91 \times 10^{-3}$ for both models.

Since we adopt fixed spatial resolution, runaway gravitational collapse cannot be followed to later stages where the gravitational length scales fall below the grid scale. To mitigate this difficulty, we adopt a sink particle algorithm in which each collapsing center is replaced by an accreting particle. Numerical details of our sink particle algorithm are described in [Paper II](#). We stop each simulation when the total mass in sink particles exceeds $0.15 M_{\text{box}}$.

We emphasize that the calculations carried out in [Paper II](#) and analyzed here are designed as a set of numerical experiments to test the theoretical ideas outlined in [Paper I](#). Additional physics, such as magnetic fields and protostellar outflows, can be included in future numerical models to make them more realistic, and therefore more directly comparable to observations. For present purposes, our intention is to keep the simplest possible setup, to facilitate physical understanding and to establish a baseline for future developments.

2.3. Definition of Critical Cores

We begin our analysis by identifying the centroids of all cores with local gravitational potential minima, which are then linked through time based on position and velocity (see Section 3.5 of [Paper II](#) for details). For each core center, we construct radial profiles of various physical quantities using [Equations \(5\) and \(6\)](#), and monitor their temporal evolution. Because instability is

expected to set in at r_{crit} according to the TES model, we define the critical time t_{crit} by

$$t_{\text{crit}} \equiv \min \{t^* \mid F_{\text{net}}(r_{\text{crit}}) < 0 \forall t \in (t^*, t_{\text{coll}})\}. \quad (22)$$

That is, the net radial force $F_{\text{net}}(r_{\text{crit}})$ acting on a ball of radius r_{crit} becomes negative at t_{crit} and stays negative until the end of the collapse at t_{coll} (see Equation (61) of Paper II for the precise definition of F_{net} and its relation to the radial acceleration.) Figure 11 of Paper II shows that t_{crit} corresponds to the epoch when the average infall speed starts to accelerate, signaling the onset of runaway collapse.

To calculate r_{crit} for simulated cores, we first fit Equation (3) to the actual profile of $\langle \delta v_r^2 \rangle_\rho^{1/2} / c_s$ for each core to determine ξ_s and p , where we use the measured central density ρ_c to convert the physical r to dimensionless ξ using Equation (4). We then calculate the dimensionless critical radius ξ_{crit} by solving the TES equations³ and convert to r_{crit} by using Equation (7). We also calculate the critical mass M_{crit} for each core in an analogous manner. Paper II found that, at t_{crit} , the critical radius becomes comparable to the “tidal radius” defined in terms of the local gravitational potential geography.

For the collapse time of each core, we use the following working definition:

$$t_{\text{coll}} \equiv \text{The time of each sink particle formation.} \quad (23)$$

The duration of collapse for each core is then defined by

$$\Delta t_{\text{coll}} \equiv t_{\text{coll}} - t_{\text{crit}}, \quad (24)$$

which can be measured for individual cores. Note that Equations (22) and (23) provide quantitative definition of the critical time and the collapse time described in Section 1.

We consider a self-gravitating core with radius r_{crit} resolved if

$$r_{\text{crit}} > N_{\text{core, res}} \Delta x, \quad (25)$$

where our standard choice is $N_{\text{core, res}} = 8$ unless otherwise mentioned. We note that this is a conservative choice amounting to resolving a core volume with $4\pi N_{\text{core}}^3/3 = 2145$ resolution elements. A core would still be marginally resolved with less restrictive choice of $N_{\text{core, res}} = 4$. Below this limit, turbulence within cores would be significantly affected by numerical dissipation and their evolution is not reliable. For example, had the resolution been higher and the dissipation lower, a core could have been dispersed by turbulence

instead of initiating collapse. With our default choice of $N_{\text{core, res}} = 8$, there are 83 and 79 cores in our entire ensemble of simulations for model M5 and M10, respectively. These numbers increase to 107 and 129 when $N_{\text{core, res}} = 4$ is adopted. It is expected that the number of resolved cores per simulation would increase with increasing numerical resolution, until the entire CMF is resolved. In Section 3.4, we will present evidence that the peak of the CMF is marginally resolved in model M5. We will further discuss numerical requirements for resolving the CMF in Appendix A.

Given that the radius of the smallest resolvable core would be $R_{\text{BE}} = N_{\text{core, res}} \Delta x$, one can use the corresponding BE mass to derive the minimum resolvable mass:

$$M_{\text{min}} = 2.43 \frac{c_s^2}{G} N_{\text{core, res}} \Delta x. \quad (26)$$

For simulations adopting a fixed mass resolution Δm , the equivalent minimum resolvable mass may be written as

$$M_{\text{min}} = \frac{4\pi N_{\text{core, res}}^3}{3} \Delta m. \quad (27)$$

In the remaining text, we use the term “critical core” to denote a ball of radius r_{crit} at $t = t_{\text{crit}}$. The radius and mass of a critical core is defined by

$$R_{\text{core}} \equiv r_{\text{crit}}(t = t_{\text{crit}}), \quad (28)$$

$$M_{\text{core}} \equiv \iiint_{r < R_{\text{core}}} \rho(t = t_{\text{crit}}) dV, \quad (29)$$

where all quantities are evaluated at $t = t_{\text{crit}}$ for each core.

3. PROPERTIES OF CRITICAL CORES

In this section, we present the physical properties of critical cores in models M5 and M10. We only include resolved cores with $R_{\text{core}} > 8\Delta x$ unless otherwise stated.

3.1. Radial Density Profiles

Figure 1 plots the normalized radial density profiles measured at $t = t_{\text{crit}}$, for 20 randomly selected cores in model M10. For comparison, we also plot the theoretical TES and BE solutions obtained using the measured central density ρ_c , sonic radius r_s , and power law index p (for the BE sphere, we assume $r_s \rightarrow \infty$). The latter two quantities are obtained by fitting Equation (3) to the measured profile of $\langle \delta v_r^2 \rangle_\rho^{1/2}$, within the tidal radius defined by the distance to the nearest saddle point of the gravitational potential (see Paper II). Figure 1 indicates that while the measured profiles are broadly consistent with the TES solutions, they cannot be described by BE spheres unless σ_{1D} (see Equation (11) for

³ We provide our Python implementation in <https://github.com/sanghyukmoon/tesphere>.

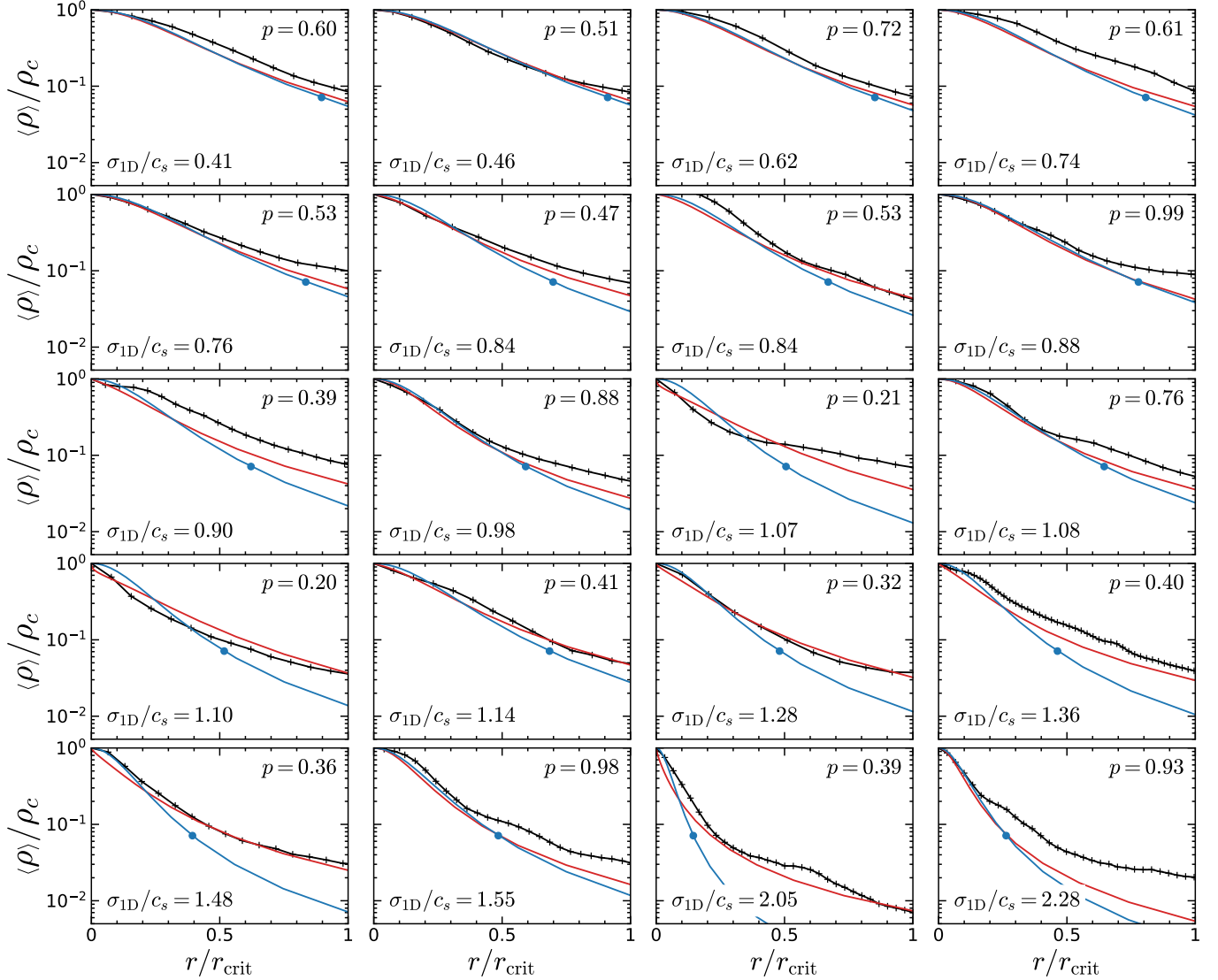


Figure 1. Radial density profiles of 20 randomly selected critical cores in model M10, arranged in an increasing order of σ_{1D} from left to right and top to bottom. In each panel, the black line with markers plots the measured density profile while the red line shows the analytic equilibrium solution of the critical TES constructed from the measured ρ_c , r_s , and p (i.e., the red line is not a fit to the black line). For comparison, we also plot the similar profile of the BE sphere in the blue line using the measured ρ_c but assuming only thermal pressure (i.e. $r_s \rightarrow \infty$). The blue circle marks the location of R_{BE} . In each panel, the density and radius are normalized by ρ_c and $R_{\text{core}} = r_{\text{crit}}$, respectively. The mass-weighted average velocity dispersion σ_{1D} and the power-law index of the fitted linewidth–size relation p are annotated in each panel.

definition) is small compared to c_s or the linewidth–size index p (see Equation (3)) is large. For the cases with supersonic turbulence within a core, density decreases at large radii much less in the simulated cores (and in the TES solutions) than in the BE solutions that match the profiles at small radius. Some cores do show moderate discrepancies from TES profiles for one or a combination of the following reasons: Departure from the spherical symmetry or the presence of nearby structures that make the gravitational force deviate from GM/r^2 ; traveling shock waves that intermittently throw a core out

of equilibrium; strong converging flows building a core in less than a sound crossing time (we come back to this in Figure 11); non-negligible rotation; a linewidth–size relation which does not conform to a single power law. Nonetheless, the overall agreement between radial density profiles of the simulated cores and TES solutions suggests that quasi-steady equilibrium structures supported by thermal and turbulent pressures naturally emerge from the interplay between supersonic turbulence and self-gravity.

3.2. Local Linewidth-size Relations and Correlation with Density

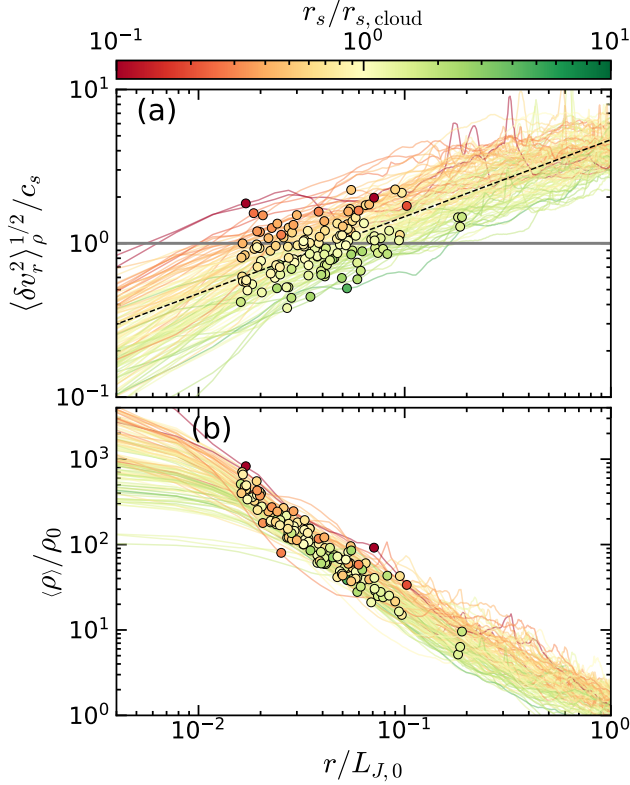


Figure 2. Radial profiles of (a) turbulent velocity dispersion and (b) density, for the critical cores in model M10. Individual lines correspond to the profiles constructed starting from the center of each core, where we include the cores with $r_{\text{crit}} \geq 4\Delta x$ (i.e., $N_{\text{core, res}} = 4$). The critical radius r_{crit} is marked with circles. The black dashed line in panel (a) plots the average linewidth-size relation, $\langle \delta v_r^2 \rangle^{1/2} / c_s = (r / r_{s, \text{cloud}})^{0.5}$, where the colors represent the ratio of the local sonic radius r_s to the average $r_{s, \text{cloud}}$ (i.e., the local deviations from the mean turbulent scaling relation). The intersection points between each colored line and the horizontal gray line representing $\langle \delta v_r^2 \rangle^{1/2} / c_s = 1$ correspond to the local sonic radius r_s for each core.

The comparison in Figure 1 suggests that turbulence affects density structure and stability to varying extents across different cores. In this section, we demonstrate how the local variations of the turbulent scaling relation affect the critical density at which collapse is triggered. To illustrate the variations in the locally-constructed linewidth-size relations, in Figure 2(a) we plot the turbulent velocity dispersion $\langle \delta v_r^2 \rangle^{1/2} / c_s$ measured for each critical core as a function of growing radius from the core center (see Equation (3)). The colors show the ratio $r_s / r_{s, \text{cloud}}$, i.e., the local sonic radius relative to

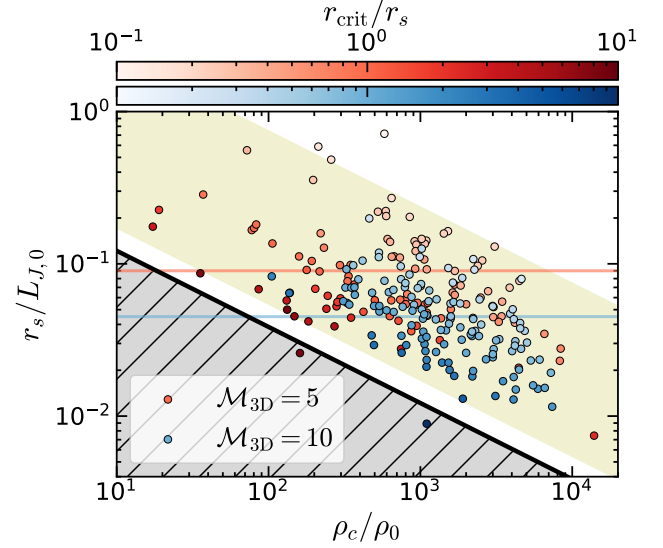


Figure 3. Local sonic radius versus central density measured for selected individual cores from model M5 (red) and M10 (blue), satisfying the resolution criterion $N_{\text{core, res}} = 4$. Black line plots Equation (31), such that a TES with $p = 0.5$ is stable at all radii when r_s and ρ_c falls in the gray shaded region. Horizontal red and blue lines correspond to $r_{s, \text{cloud}}$ (defined in Equation (21)) for model M5 and M10, respectively. Circles are colored by r_{crit} / r_s , where $\sigma_{1D} / c_s \approx 0.8(r_{\text{crit}} / r_s)^{1/2}$ from Equation (12). The yellow shaded band is the region where σ_{1D} / c_s is between 0.3 (upper edge) and 2 (lower edge).

the cloud average defined in Equation (21). Figure 2(a) shows that the turbulent velocity dispersion measured at a given size scale varies up to a factor of a few above and below the average relation given by $c_s (r / r_{s, \text{cloud}})^{0.5}$. Alternatively, it implies that the locally measured sonic radius, r_s , exhibits order of magnitude variations around $r_{s, \text{cloud}}$.

Large spatial variations in the strength of turbulence shown in Figure 2(a) suggest that the necessary density for cores to collapse would differ considerably from core to core. Figure 2(b) plots the density profiles of critical cores normalized to the average cloud density ρ_0 and the associated Jeans length $L_{J,0}$, with the same color coding as in Figure 2(a). The noticeable vertical color gradients suggest that cores forming in more turbulent regions (i.e., smaller r_s) overall have higher densities when compared at a given radius.

To illustrate this point more clearly, in Figure 3 we plot the central density ρ_c versus the local sonic radius r_s for all critical cores in models M5 and M10. It shows that, for critical cores, r_s and ρ_c are anticorrelated, meaning that cores in regions of strong turbulence need to reach higher densities to initiate collapse. The distribution shown in Figure 3 also exhibits scatter

in the direction perpendicular to the overall anticorrelation, which, together with the overall anticorrelation, can be understood in the framework of TESs as follows.

Assuming $p = 0.5$, Equations (4) and (13) yield an expression for the central density required for a core to collapse, depending on its level of turbulence and the local sonic radius:

$$\frac{\rho_c}{\rho_0} \approx \frac{1}{4\pi^2} \left(\frac{r_s}{L_{J,0}} \right)^{-2} \left[2.42 + 4 \left(\frac{\sigma_{1D}}{c_s} \right)^{-2} \right]^2. \quad (30)$$

We note that the term in the square bracket can be alternatively expressed by $2.42 + 6.6r_s/r_{\text{crit}}$, using Equation (12) with $\eta_d = 0.9$ and $p = 0.5$. Additionally, it is worth noting that the mean cloud density ρ_0 only enters Equation (30) because we write r_s in units of $L_{J,0} = c_s(\pi/G\rho_0)^{1/2}$. Thus, Equation (30) indicates that ρ_c is overall proportional to r_s^{-2} , with scatter from varying σ_{1D}/c_s modulated by relative core size r_{crit}/r_s , consistent with the trend observed in Figure 3. At fixed r_s , larger and more turbulent cores (which go together following $\sigma_{1D}/c_s \approx 0.8(r_{\text{crit}}/r_s)^p$) have lower ρ_c/ρ_0 . As emphasized in Paper I and Paper II, core size is subject to the local gravitational potential environment.

It is worth noting that almost all critical cores fall under the region of parameter space where $\sigma_{1D}/c_s \in [0.3, 2]$ (shown as yellow shaded band in Figure 3). That is, we find neither purely thermal cores with $\sigma_{1D} \ll c_s$, nor highly turbulent cores with $\sigma_{1D} \gg c_s$. The center of the distribution shown in Figure 3 lies roughly along $\xi_s \sim 9$, corresponding to $\sigma_{1D}/c_s = 0.78$. For a $p = 0.5$ TES, the critical radius becomes identical to the sonic radius when $\xi_s \sim 9$ (see Figure 4(a) of Paper I). This means that cores in our simulations on average have $r_{\text{crit}} \sim r_s$ at the onset of collapse. We discuss physical reasons for this below.

Paper II found that collapse occurs when r_{crit} decreases below the tidal radius r_{tidal} , which is set by local geography of the gravitational potential. Our results therefore imply that critical cores generally satisfy $r_{\text{crit}} \sim r_s \sim r_{\text{tidal}}$. Indeed, r_s is the scale at which the nonlinear structures are expected, which may in turn determine the size of the local potential well characterized by r_{tidal} .

We additionally note that, for a given r_s , there exists a minimum central density below which all TES solutions are stable (Paper I). For $p = 0.5$, this minimum can be obtained by taking the $\sigma_{1D} \rightarrow \infty$ limit in Equation (30), leading to

$$\frac{\rho_{c,\text{min}}}{\rho_0} = 0.148 \left(\frac{r_s}{L_{J,0}} \right)^{-2}, \quad (31)$$

or equivalently $\rho_{c,\text{min}} = 0.46(c_s/r_s)^2/G$. This is plotted in a solid black line in Figure 3. In the presence of tur-

bulence satisfying Equation (3) with $p = 0.5$, the theory predicts that collapse cannot occur in the shaded region below this borderline. The absence of critical cores from our simulations in the shaded region is consistent with this theoretical prediction. As shown in Figure 16 of Paper II, cores generally form in this stable regime and then evolve diagonally through the borderline, until the critical conditions are satisfied at various locations within the yellow shaded region of the parameter space shown in Figure 3.

3.3. Distribution of Turbulence Parameters and Core Densities

Figure 4 plots the distribution of p , r_s , ξ_s , and σ_{1D} from all critical cores in models M5 and M10. The median values of p (the index of the fitted linewidth–size relation in Equation (3)) are 0.41 and 0.56 for model M5 and M10, respectively, roughly consistent with the expected average slope of 0.5 resulting from the initial velocity power spectrum. However, the distribution is rather broad, such that individual cores can have diverse values of p ranging between ~ 0.2 – 0.8 . Cores in model M5 have overall slightly smaller values of p compared to those forming in model M10.

Due to higher initial \mathcal{M}_{3D} , the sonic radius of the cores is generally smaller in model M10. The median values are $r_s = 8.7 \times 10^{-2} L_{J,0}$ and $5.0 \times 10^{-2} L_{J,0}$ for model M5 and M10, respectively, entirely consistent with what expected from the initial box-scale Mach number (Equation (21)).⁴

While cores in model M10 have overall smaller r_s than model M5, they tend to have higher ρ_c , presumably due to the stronger turbulent compression of core-forming regions at higher cloud-scale Mach number. This makes the distribution of the dimensionless sonic radius $\xi_s = (4\pi G\rho_c)^{1/2} r_s/c_s$ (which determines the structure of forming cores; see Paper I) not very different between models M5 and M10. The median and ± 34.1 th percentile range of ξ_s for the entire ensemble of cores is $9.5^{+9.2}_{-4.3}$.

Figure 4(d) shows that most cores in models M5 and M10 have subsonic or transonic velocity dispersions, as noted in connection to Figure 3. The level of turbulence in our critical cores is consistent with the kinematics of observed prestellar cores (e.g., Lee et al. 1999, 2001; Foster et al. 2009; Friesen et al. 2009, 2010; Lee et al.

⁴ Although the box-averaged Mach number has decayed from its initial \mathcal{M}_{3D} by the time most cores form and collapse, we find the energy loss is predominantly at large scales and the velocity structure function at core scales is in fact consistent with the initial condition (see Figure 2(a) as well as Figure 15 of Paper II).

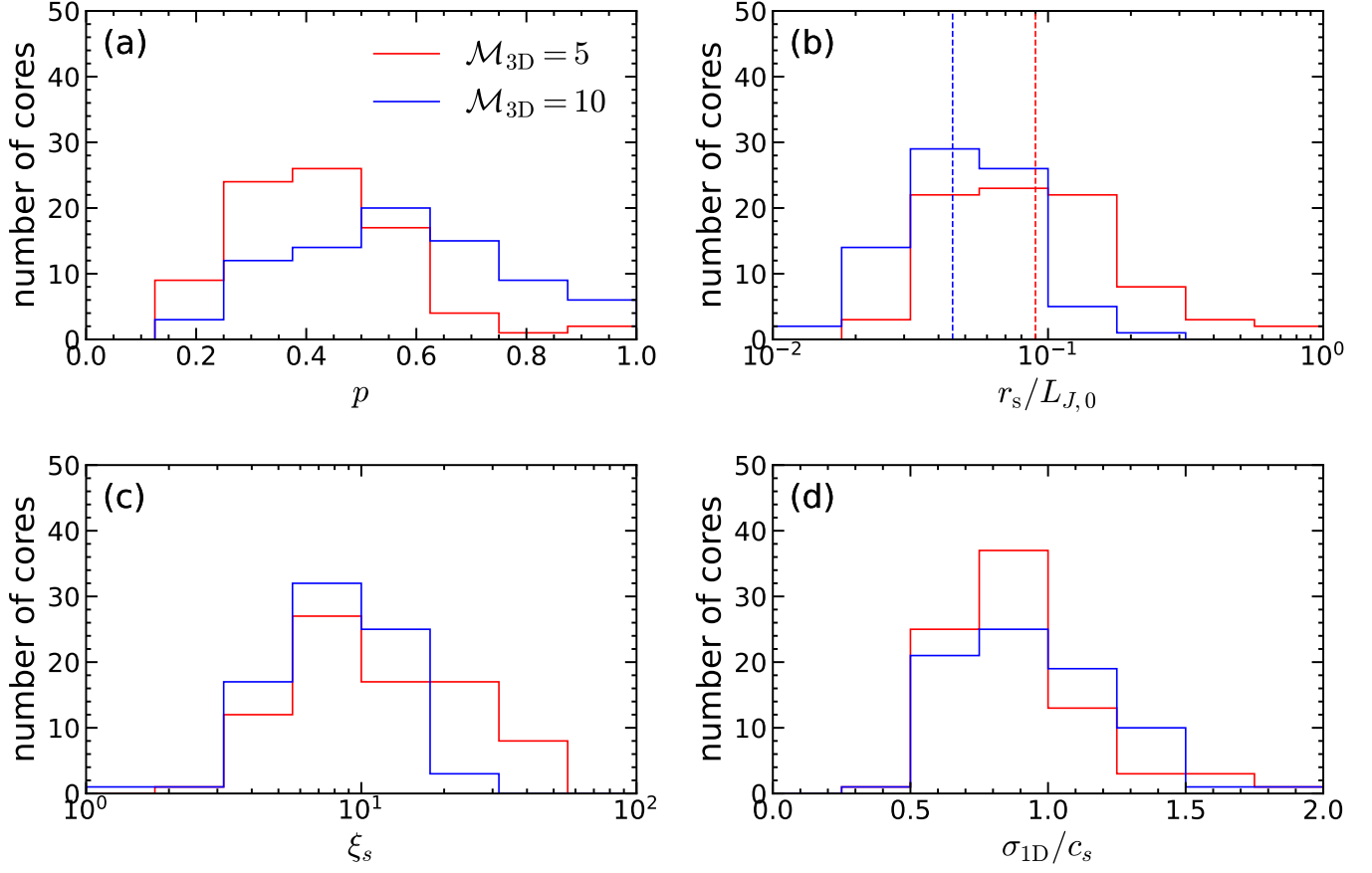


Figure 4. Distributions of dynamical properties in all critical cores from models M5 (red) and M10 (blue). Shown are (a) the power-law exponent p of the linewidth-size relation, (b) the sonic radius r_s , (c) the dimensionless sonic radius ξ_s (see Equation (4)), and (d) the mass-weighted average velocity dispersion σ_{1D} (Equation (11)). The vertical dotted lines in panel (b) mark the initial sonic radius $r_{s,\text{cloud}}$ defined in (Equation (21)) which is expected from the large-scale k^{-2} velocity power spectrum.

2014; Storm et al. 2016; Keown et al. 2017; Kirk et al. 2017; Tang et al. 2018; Chen et al. 2019; Chung et al. 2019; Kerr et al. 2019; Choudhury et al. 2021; Chung et al. 2021; Li et al. 2023; Yoo et al. 2023). The median and ± 34.1 th percentile range of σ_{1D}/c_s is $0.88^{+0.30}_{-0.18}$.

Figure 5 plots the distribution of densities of cores at their critical time: Central ρ_c , edge ρ_e (defined as the value at $r = R_{\text{core}}$), and mean $\bar{\rho} = M_{\text{core}}/(4\pi R_{\text{core}}^3/3)$, as well as the center-to-edge contrast ρ_c/ρ_e . This makes clear that cores form at a wide range of densities, with a typical value around $\bar{\rho} \sim 10^2 \rho_0$, corresponding to $\bar{n}_{\text{H}_2} \sim 10^4 \text{ cm}^{-3}$ for a cloud with average molecular hydrogen number density $n_{\text{H}_2,0} = 10^2 \text{ cm}^{-3}$. A caveat is that the distribution is likely to become incomplete somewhere in the regime $\bar{\rho}/\rho_0 \gtrsim 10^2\text{--}10^3$; we refer the reader to Section 3.3 of Paper II for a discussion of our resolution criteria. The distribution of center-to-edge density contrast is narrow, peaking at $\rho_c/\rho_e \sim 10\text{--}30$. Some cores have a center-to-edge contrast of less than

14 because they have excess mass at their edge compared to isolated TES solutions (e.g., Figure 1).

It is interesting to reexamine the distribution of ρ_c in models M5 and M10 by using Equation (30). Neglecting the local variations of r_s and instead adopting the “average” value $r_s = r_{s,\text{cloud}}$ defined in Equation (21), one can relate the required central density to a cloud’s virial parameter and Mach number as

$$\frac{\rho_c}{\rho_0} \approx 7.56 \times 10^{-2} \left[2.42 + 4 \left(\frac{\sigma_{1D}}{c_s} \right)^{-2} \right]^2 \alpha_{\text{vir,box}} \mathcal{M}_{3D}^2, \quad (32)$$

where an implicit assumption is $p = 0.5$ inherited from using Equation (13). For a cloud with given $\alpha_{\text{vir,box}}$ and \mathcal{M}_{3D} , Equation (32) has a lower bound,

$$\frac{\rho_{c,\text{min}}}{\rho_0} = 0.443 \alpha_{\text{vir,box}} \mathcal{M}_{3D}^2, \quad (33)$$

in the limit of $\sigma_{1D} \rightarrow \infty$. For models M5 and M10, Equation (33) yields $\rho_{c,\text{min}} = 18\rho_0$ and $74\rho_0$, respectively,

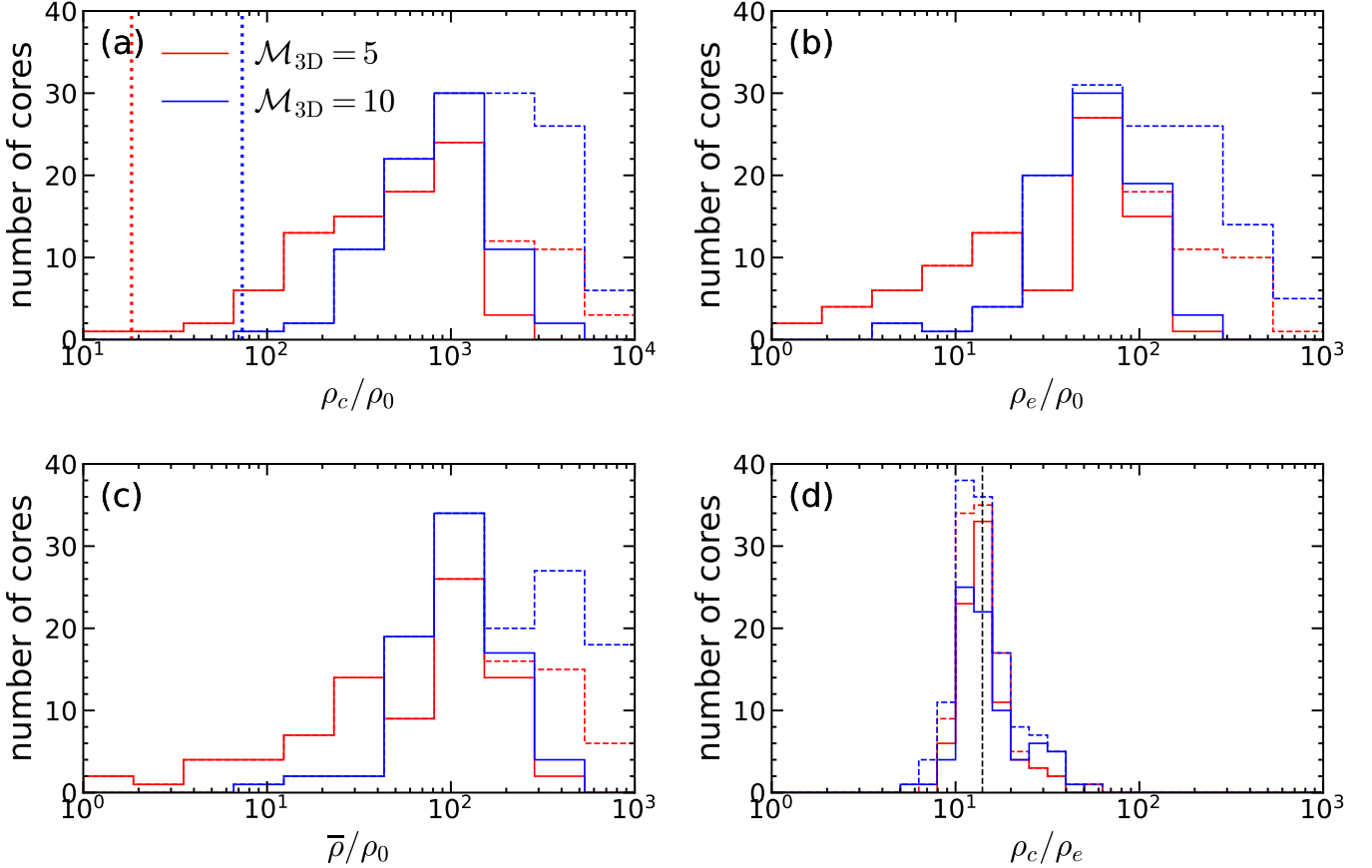


Figure 5. Distribution of density values in all critical cores from models M5 (red) and M10 (blue), satisfying the resolution criterion (Equation (25)) with the standard choice of $N_{\text{core,res}} = 8$ (solid histograms) and the relaxed choice $N_{\text{core,res}} = 4$ (dashed histograms). Shown are (a) center, (b) edge, (c) mean densities relative to the mean density in the box, and (d) the center-to-edge density contrast. In (a), vertical dotted lines plot the theoretical prediction for the minimum central density allowing instability, assuming $p = 0.5$ (Equation (33)). The vertical dotted line in the panel (d) marks $\rho_c/\rho_e = (\rho_c/\rho_e)_{\text{BE}} = 14$.

which are intriguingly similar to the lower edges of the central density distribution shown in Figure 5(a). For transonic cores with $r_{\text{crit}} = r_s$ (i.e., $\sigma_{1D} \approx 0.8c_s$, representative in Figure 4(d)), Equation (32) yields $\rho_c = 236\rho_0$ and $943\rho_0$ for models M5 and M10, respectively, which are closer to typical central densities of cores.

3.4. Core Mass and Radius Distributions

Figure 6(a) plots the mass function of critical cores, defined as the number of cores per logarithmic interval of M_{core} , for models M5 and M10. We introduce a new term “critical core mass function” (CCMF) to distinguish our mass function, which is specifically constructed at t_{crit} of each core, from observed CMFs consisting of cores at various evolutionary stages. We also plot the distribution of the core radius in Figure 6(b). We remind the reader that these cores are defined at their own critical time, which occurs at a different point in the simulation for each core. Although the CCMF shows marginal evidence of a peak, the location of a peak is only a factor of

~ 2 higher than $M_{\text{min}}/M_{J,0} = 2.42 \times 10^{-2} (N_{\text{core,res}}/8)$ if we adopt $N_{\text{core,res}} = 8$ in Equation (26), requiring some caution in interpretation. If we relax the criterion for cores being resolved from $N_{\text{core,res}} = 8$ to 4, the nominal resolved mass drops to $M_{\text{min}}/M_{J,0} = 1.21 \times 10^{-2}$. While the CCMF peak position for model M5 does not vary much after including these lower mass cores, the peak shifts toward lower mass for model M10. We note, however, that at higher resolution, turbulent dissipation would have been lower in these less resolved cores and they would have been prevented from collapsing.

If cores were supported only by thermal pressure, one might expect a characteristic mass for collapse in a turbulent simulation to be given by the BE mass in Equation (2) when $\bar{\rho}$ is set equal to the characteristic post-shock value based on the large scale Mach number in the cloud,

$$M_{\text{char,th}} = 1.86 \frac{c_s^3}{G^{3/2} \rho_0^{1/2} \mathcal{M}_{3D}} = 0.334 \frac{M_{J,0}}{\mathcal{M}_{3D}} \quad (34)$$

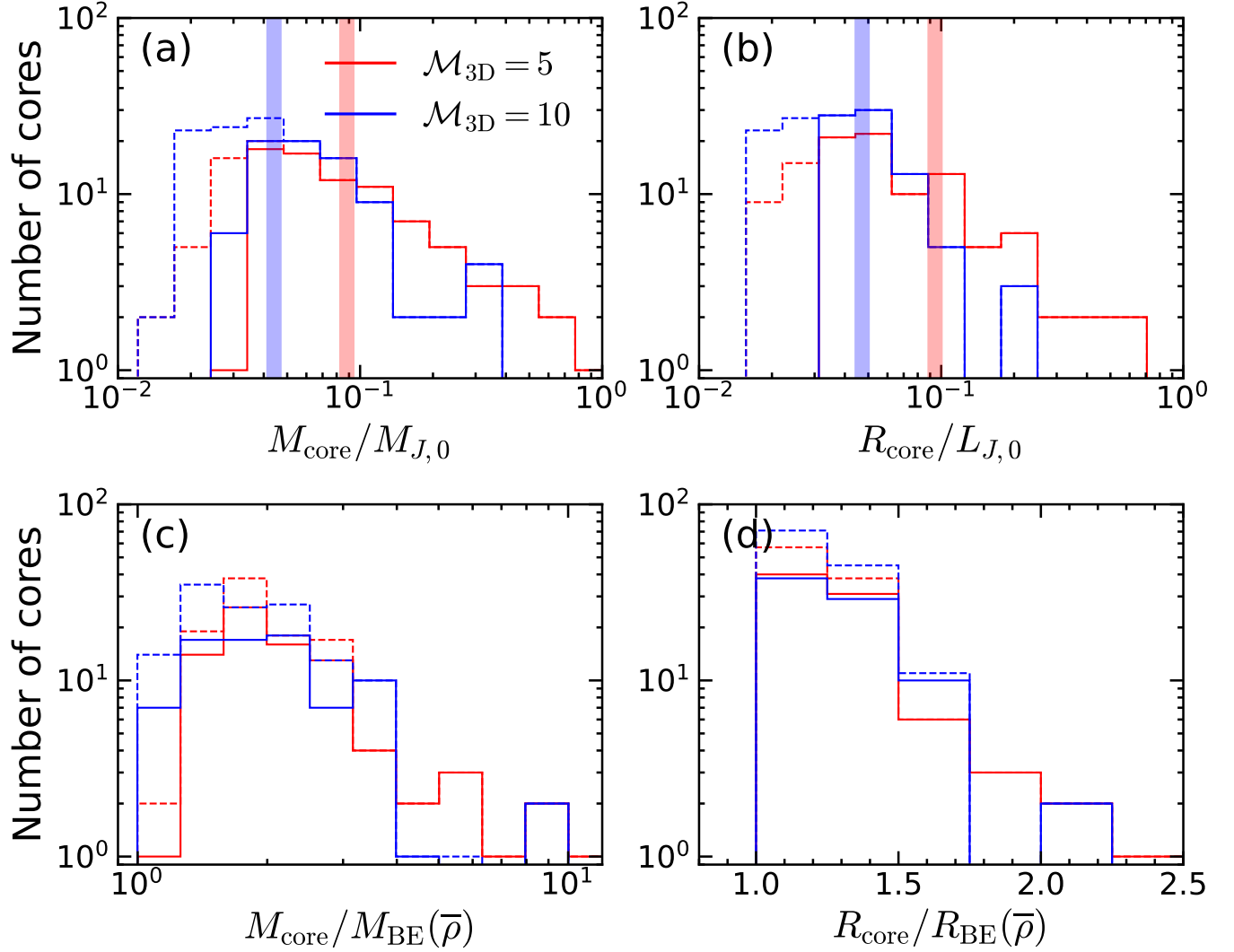


Figure 6. Distribution of mass and radius of critical cores in models M5 (red) and M10 (blue), satisfying the resolution criterion (Equation (25)) with the standard choice of $N_{\text{core,res}} = 8$ (solid histograms) and the relaxed choice $N_{\text{core,res}} = 4$ (dashed histograms). (a) The CCMF; bin lower limits for mass are at M_{min} from Equation (26) for a chosen $N_{\text{core,res}}$. (b) The distribution of core radius, where by definition $R_{\text{core}} = r_{\text{crit}}$ at $t = t_{\text{crit}}$. Lower limits are at $N_{\text{core,res}}\Delta x$. For (a) and (b) shaded bands mark $M_{\text{char,trb}}$ and $R_{\text{char,trb}}$ defined in Equation (35) and Equation (36) for $\mathcal{M}_{3D} = 5$ and 10, respectively (see text for details). (c) The distribution of the ratio between the core mass and the BE mass evaluated at the average core density. (d) The distribution of the ratio between the core radius and the BE radius evaluated at the average core density.

(e.g. Gong & Ostriker 2011; Chen & Ostriker 2014; Haugbølle et al. 2018). Allowing for turbulent support of cores, this would be generalized to

$$M_{\text{char,trb}} \equiv M_{\text{crit}}(\bar{\rho} = \rho_0 \mathcal{M}_{3D}^2) \approx 0.334 \frac{M_{J,0}}{\mathcal{M}_{3D}} \left(1 + \frac{1}{2} \frac{\sigma_{1D}^2}{c_s^2} \right) \quad (35)$$

where M_{crit} is the critical TES mass including turbulent support and we use Equation (10) in the second line for $p = 0.5$. Taking $\sigma_{1D} = 0.8c_s$ as a representative value in Figure 4(d), Equation (35) indicates that the characteristic mass including turbulent support is only

slightly higher than the BE mass at the post-shock density given above, $M_{\text{char,trb}} = 1.32M_{\text{char,th}}$. For $\mathcal{M}_{3D} = 5$ and 10, this corresponds to $M_{\text{char,trb}} = 8.8 \times 10^{-2} M_{J,0}$ and $4.4 \times 10^{-2} M_{J,0}$, respectively, which are plotted in vertical shaded bands in Figure 6(a). For model M5 where the peak of the CCMF appears to be marginally resolved, the apparent peak occurs at $\sim 0.5M_{\text{char,trb}}$. Scaling from this result, the expected peak position for model M10 would then be $0.5M_{\text{char,trb}} \sim 2.2 \times 10^{-2} M_{J,0}$. This is close to CCMF peak for the dashed pdf, which adopts $N_{\text{core,res}} = 4$. However, we consider this too close to $M_{\text{min}} = 2.42 \times 10^{-2} M_{J,0} (N_{\text{core,res}}/8)$ to be properly

resolved. Both higher resolution simulations, possibly aided by adaptive mesh refinement techniques with careful refinement criteria, and extension of the parameter space to higher Mach numbers, would be required to convincingly address the questions of (1) whether or not there exists a numerically converged peak in the CCMF, and (2) whether the peak is consistent with theoretical hypotheses (see [Appendix A](#) for related discussion).

[Figure 6\(b\)](#) plots a similar distribution for core radius. Again, the $\mathcal{M}_{3D} = 5$ histogram suggests that the peak in the distribution occurs at half of the characteristic radius

$$R_{\text{char, trb}} \equiv R_{\text{crit}}(\bar{\rho} = \rho_0 \mathcal{M}_{3D}^2) \approx 0.430 \frac{L_{J,0}}{\mathcal{M}_{3D}} \left(1 + \frac{1}{2} \frac{\sigma_{1D}^2}{c_s^2}\right)^{1/3}. \quad (36)$$

[Figure 6\(c\)](#) shows M_{core} is roughly a factor of ~ 2 higher than M_{BE} measured at the average density $\bar{\rho}$, although a few cores have even higher ratio. While this enhancement can be attributed to turbulent support (i.e., $M_{\text{crit}} \geq M_{\text{BE}}$, as in [Equation \(10\)](#)), some cores have additional mass excess due to rapid core building, as we will show later in [Figure 11](#).

Finally, [Figure 6\(d\)](#) plots the distribution of $R_{\text{core}}/R_{\text{BE}}$ which is equivalent to $r_{\text{crit}}/R_{\text{BE}}$ for critical cores. It shows that the critical radius is larger than the BE radius by no more than a factor of ~ 2 , which is expected for transonic cores ([Equation \(9\)](#)).

In [Figure 7\(a\)](#), we plot the ratio $R_{\text{core}}/R_{\text{BE}}(\bar{\rho})$ as a function of the one-dimensional Mach number σ_{1D}/c_s . Overall, critical cores follow the curves defined by the TES solutions, although the measured ratio is slightly ($\sim 10\%$) offset to higher values due to enhanced $\bar{\rho}$ compared to strict equilibrium ([Figure 7\(b\)](#)); we shall explain a potential reason for this in [Figure 11](#). It is worth noting that, even though the TES model in principle extends to either a purely thermal regime with $\sigma_{1D} \ll c_s$ or a highly turbulent regime with $\sigma_{1D} \gg c_s$, all of the critical cores in our simulations are found in the regime $0.5 < \sigma_{1D}/c_s < 2$. We find no critical cores with either very low or very high levels of internal turbulence. This is because 1) cores have a turbulent origin and are able to initiate collapse before σ_{1D} completely dissipates, so that there are no purely thermal cores; 2) highly turbulent cores would be self-destructive, in the sense of being torn apart before they can collapse. In particular, [Figure 8\(d\)](#) of [Paper I](#) shows for TES solutions that the flow crossing time is shorter than the average free-fall time for cores with $\sigma_{1D}/c_s > 2$. As a result, the critical cores formed in our simulations are largely transonic, which is also likely the case for real cores.

3.5. Core Shape Distributions

It is well known from observations ([Myers et al. 1991](#); [Ryden 1996](#); [Jones et al. 2001](#); [Tassis 2007](#); [Lomax et al. 2013](#)) and from simulations both with ([Gammie et al. 2003](#); [Basu & Ciolek 2004](#); [Li et al. 2004](#); [Nakamura & Li 2008](#); [Chen & Ostriker 2018](#)) and without ([Klessen & Burkert 2000](#); [Offner & Krumholz 2009](#); [Gong & Ostriker 2011](#)) magnetic fields that dense cores at various evolutionary stages are intrinsically triaxial in terms of their density distribution.

In this section, we take advantage of our dynamical identification of t_{crit} ([Equation \(22\)](#)) and t_{coll} ([Equation \(23\)](#)) to characterize this shape distribution at the beginning and at the end of the collapse. To do this, we calculate the moment of inertia tensor $I_{ij} \equiv \int \rho x_i x_j dV$ by integrating over a sphere of radius R_{core} centered at each core, and then find its three eigenvalues $a \geq b \geq c$. [Figure 8](#) plots the axis ratios b/a and c/a for cores in model M10 satisfying $N_{\text{res, core}} = 8$, taken at t_{crit} and t_{coll} . The mean and standard deviation for the axis ratios are $b/a = 0.73 \pm 0.12$ and $c/a = 0.45 \pm 0.12$ at t_{crit} , and $b/a = 0.60 \pm 0.18$ and $c/a = 0.39 \pm 0.16$ at t_{coll} , indicating that the cores are generally triaxial at all times with a broad axis ratio distribution. The overall smaller axis ratios at t_{coll} compared to at t_{crit} suggest that the cores become more elongated as collapse progresses, as expected for gravitational collapse ([Lin et al. 1965](#)).

We note that the main body of the analysis presented in this work and in [Paper II](#) is based on angle-averaged radial profiles rather than density or gravitational potential contours. The equation of motion for the angle-averaged radial velocity ([Equation \(61\)](#) of [Paper II](#)) does not itself require the density distribution to be spherically symmetric. The TES model, does, however, involve additional assumptions that the mass-weighted mean rotational velocity is zero and that the mass-weighted turbulent velocities are statistically isotropic ([Paper I](#)), which may be violated for triaxial cores due to anisotropic density weighting. Nonetheless, the overall agreement between the TES model and our simulated cores (e.g., [Figures 1](#) and [7](#)) suggests that the TES model provides a reasonable approximation.

4. ACCRETION RATES AND EVOLUTIONARY STAGES

In our simulations, cores form in regions where velocity fields are locally converging. From a Eulerian perspective, the mass contained within a fixed radius R_{core} grows in time, reaching M_{core} at $t = t_{\text{crit}}$ (see [Equations \(28\)](#) and [\(29\)](#) for definitions of R_{core} and M_{core}). To estimate the time taken to build up M_{core} within

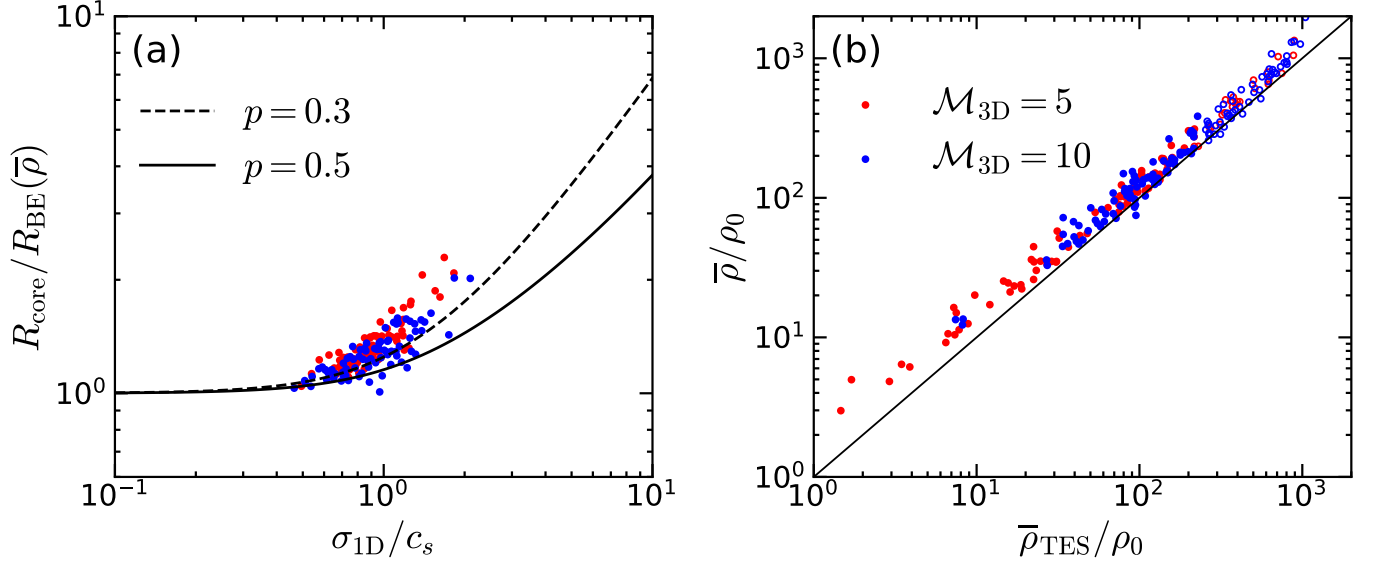


Figure 7. Comparison of measured core properties with TES solutions, for the critical cores in models M5 (red) and M10 (blue). (a) The ratio of the core radius to the BE radius at the average density as a function of the turbulent Mach number. The solid and dashed lines correspond to the loci of TESs with $p = 0.5$ and 0.3 , respectively. (b) The average density within R_{core} versus the predicted density of $p = 0.5$ TESs (Equation (14)). Filled and open symbols denote critical cores satisfying the resolution criterion with $N_{\text{res,core}} = 8$ and 4, respectively.

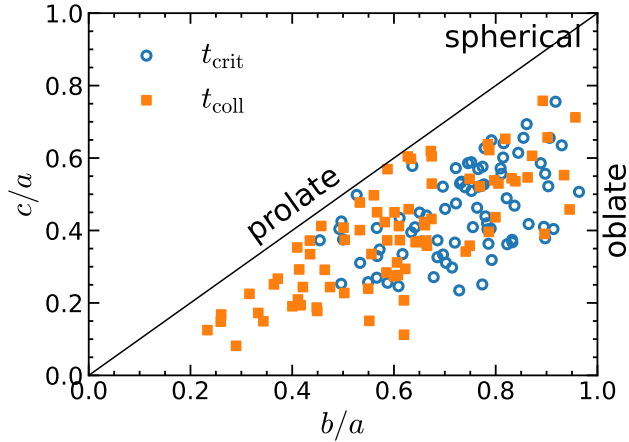


Figure 8. Axis ratio distribution for cores in model M10 at t_{crit} (blue circles) and t_{coll} (orange squares). a , b , and c are the three eigenvalues (largest to smallest) of the moment of inertia tensor calculated within R_{core} .

R_{core} , we monitor the mass inflow rate

$$\dot{M}_{\text{in}} \equiv -\langle 4\pi r^2 \rho v_r \rangle = -4\pi r^2 \langle \rho \rangle \langle v_r \rangle_\rho \quad (37)$$

for each core. Figure 9(a) plots the time evolution of $\dot{M}_{\text{in}}(r = R_{\text{core}})$ for 20 randomly selected cores, showing that the mass accretion rate is roughly constant in time, although some cores show a slightly increasing trend.

Motivated by the limited variations in \dot{M}_{in} over time, we define the duration of the core building stage as

$$\Delta t_{\text{build}} \equiv \frac{M_{\text{core}}}{\dot{M}_{\text{in}}(r = R_{\text{core}}, t = t_{\text{crit}})}. \quad (38)$$

Figure 9(c) shows that the inflow rate responsible for the core building, $\dot{M}_{\text{in}}(r = R_{\text{core}}, t = t_{\text{crit}})$, peaks at around $\sim 3c_s^3/G$. The time required to build a single BE mass core is therefore $M_{\text{BE}}/[3c_s^3/G] \sim t_{\text{ff}}$. Because actual core mass at t_{crit} is generally larger than M_{BE} (Figure 6(c)), the core building takes $\Delta t_{\text{build}} \gtrsim t_{\text{ff}}$ as shown in Figure 10(a).

Also interesting is to compare the building time to the sound crossing time R_{core}/c_s . Figure 11(a) shows that most cores are built within a single sound crossing time, meaning that core building occurs dynamically rather than quasi-statically, consistent with a large scatter in the measured net force before the critical time (see Figure 11 and 14 of Paper II). Nonetheless, the core mass M_{core} measured at t_{crit} is comparable to the critical TES mass M_{crit} within a factor of ~ 2 (see Figure 11(b)), indicating that most cores manage to approach a quasi-equilibrium at the end of the building stage (see also Figure 1 for radial density profiles). Interestingly, Figure 11(b) shows that the ratio $M_{\text{core}}/M_{\text{crit}}$ increases with decreasing building time for $\Delta t_{\text{build}} < R_{\text{core}}/c_s$, whereas for $\Delta t_{\text{build}} > R_{\text{core}}/c_s$ the ratio is relatively constant at $M_{\text{core}} = 1.3M_{\text{crit}}$ (for comparison, the median ratio is $M_{\text{core}}/M_{\text{crit}} = 1.6$ for cores with $t_{\text{build}} < R_{\text{core}}/c_s$). This suggests that the cores built rapidly by strong converging flows may never go through a quasi-equilibrium configuration before collapsing; however, such cases are rare in our simulations. The dynamic nature of core building may partially ex-

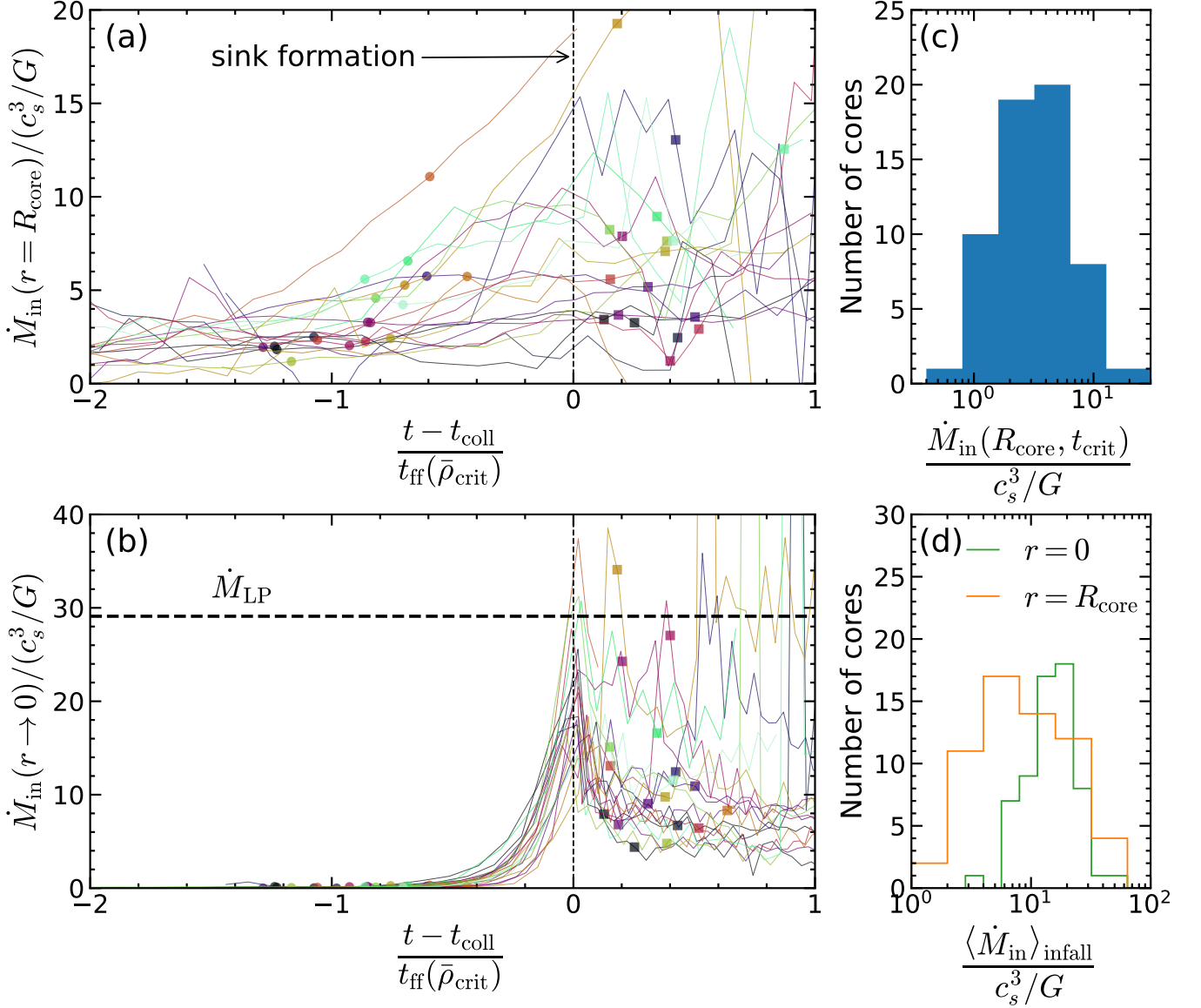


Figure 9. Accretion history and statistics. Left panels show temporal histories of the accretion rate for 20 randomly selected cores in model M10, measured at (a) $r = R_{\text{core}}$ and (b) $r = 0$ (see the main text for definitions). For each core, time is measured from t_{coll} (when a sink particle forms), such that negative (positive) time corresponds to the prestellar (protostellar) stage, and is normalized by the free-fall time at the mean core density $\bar{\rho}_{\text{crit}} \equiv 3M_{\text{core}}/(4\pi R_{\text{core}}^3)$. Circles and squares mark t_{crit} and $t_{*,100}$ for each individual core, the latter of which is undefined for some sink particles that merge with another particle. The horizontal dashed line in panel (b) marks the asymptotic accretion rate of the LP flow defined in Equation (40). Right panels show accretion statistics for all cores in model M10. (c) The distribution of the inflow rate measured at $r = R_{\text{core}}$ and $t = t_{\text{crit}}$. (d) The distribution of the time-averaged accretion rates at $r = R_{\text{core}}$ (orange histogram) and $r = 0$ (green histogram). The average is taken during the interval $[t_{\text{coll}}, t_{*,100}]$, except some cases where core tracking stopped before $t_{*,100}$.

plain why some cores show radial profiles deviating from the equilibrium solution (Figure 1).

To monitor the collapsing flow near the center and subsequent accretion onto the sink particle, we also measure the mass accretion rate at the center, $\dot{M}_{\text{in}}(r \rightarrow 0)$. We have used the notation $\dot{M}_{\text{in}}(r \rightarrow 0)$ because, strictly speaking, the accretion rate must be formally zero at $r = 0$. In practice, we take $\dot{M}_{\text{in}}(r \rightarrow 0)$ to be Equa-

tion (37) evaluated at $r = \Delta x$ before a sink particle forms (i.e., $t < t_{\text{coll}}$), whereas we use the sink particle accretion rate defined by

$$\dot{M}_{\text{sink}}(t) \equiv \frac{M_{\text{sink}}(t) - M_{\text{sink}}(t - 10^{-3}t_{J,0})}{10^{-3}t_{J,0}} \quad (39)$$

to represent $\dot{M}_{\text{in}}(r \rightarrow 0)$ after t_{coll} . Figure 9(b) shows that $\dot{M}_{\text{in}}(r \rightarrow 0)$ is essentially zero before t_{crit} , while

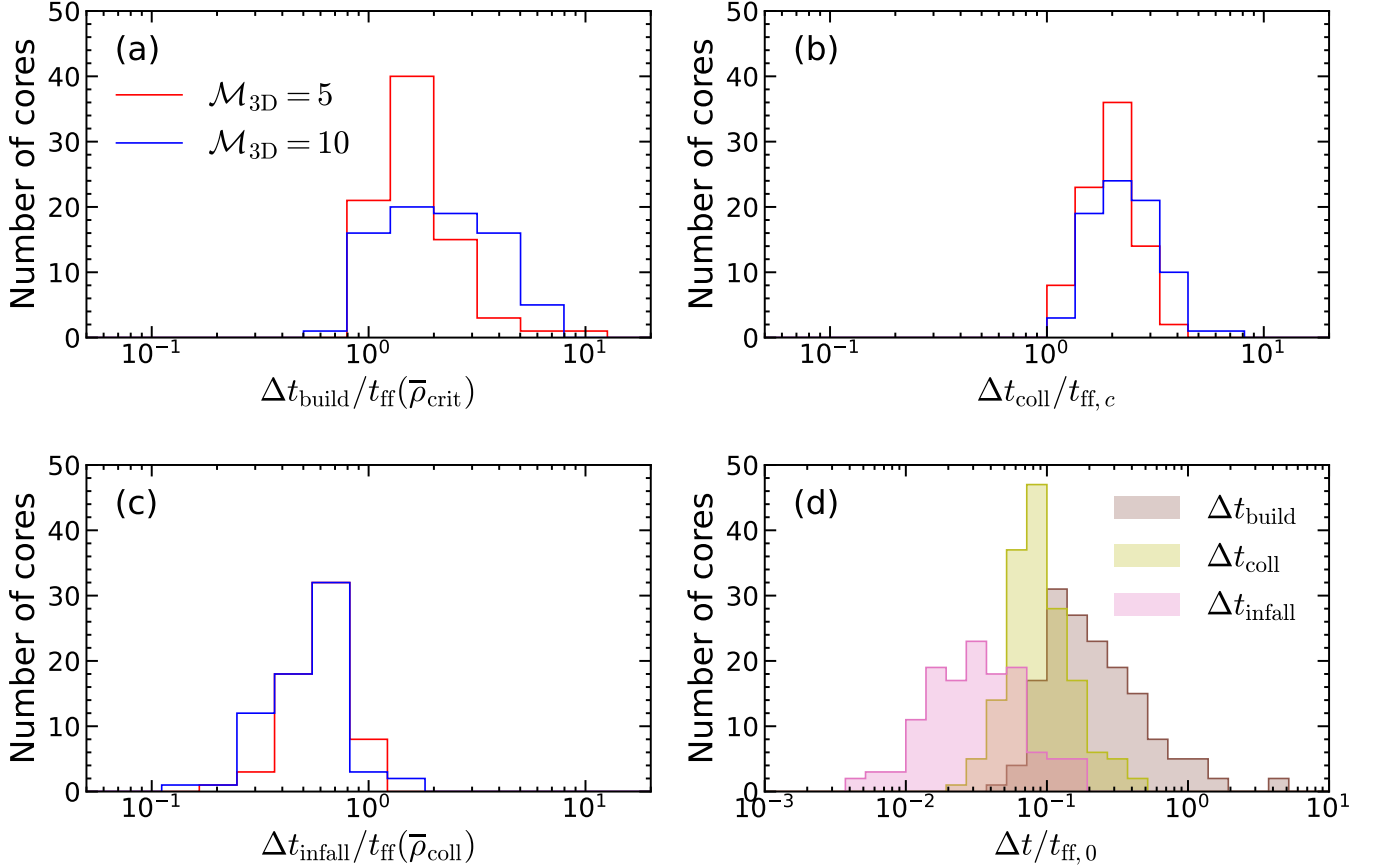


Figure 10. The distributions of the measured durations that a core spends in (a) the core building stage (Δt_{build}), (b) the core collapse stage (Δt_{coll}), and (c) the envelope infall stage (Δt_{infall}), for cores in model M5 (red) and M10 (blue). The timescales are normalized by gravitational free-fall times at a density appropriate for each stage. (d) The comparison of the combined distributions of Δt_{build} (brown), Δt_{coll} (yellow), and Δt_{infall} (pink) for all cores in models M5 and M10; here the timescales are given in units of $t_{\text{ff},0}$, which is $\sim 3\text{--}6$ Myr under typical GMC conditions (Equation (19)).

it rapidly increases as $t \rightarrow t_{\text{coll}}$, approaching (but not reaching) the corresponding value of the LP similarity solution,

$$\dot{M}_{\text{LP}} = 29.1 \frac{c_s^3}{G}, \quad (40)$$

although our limited output time resolution prevents us from measuring $\dot{M}_{\text{in}}(r \rightarrow 0)$ very close to t_{coll} . We note that the rapid increase of $\dot{M}_{\text{in}}(r \rightarrow 0)$ does not occur immediately after t_{crit} , indicating that it takes time for the wave of outside-in collapse to reach the center.

For a centrally concentrated sphere initially at rest, it takes a central free-fall time $t_{\text{ff},c} \equiv [3\pi/(32G\rho_c)]^{1/2}$ to form a singularity at the origin when the pressure is negligible. Figure 10(b) shows that the duration of the core collapse stage Δt_{coll} defined in Equation (24) is narrowly distributed around the median $\Delta t_{\text{coll}} = 2t_{\text{ff},c}$, indicating that the collapse monitored in our simulations is two times slower than a pressureless free-fall. We note that this is quantitatively consistent with the predicted

collapse duration from the measured net force within cores (see Section 5.3 of Paper II).

After a sink particle forms at t_{coll} , the accretion rate at the center quickly declines and remains roughly constant at a level a few times smaller than \dot{M}_{LP} . This is because only the very central part of the flow manages to reach the LP asymptotic solution (Hunter 1977; Foster & Chevalier 1993; Gong & Ostriker 2009). Due to the continued accretion, the mass of a sink particle grows roughly linearly with time.

We define the time $t_{*,100}$ as the instant at which $M_{\text{sink}} = M_{\text{core}}$. This time is when all the progenitor core mass has fallen to the sink (i.e., core-to-star formation efficiency of 100%)⁵. The period of time between t_{coll} and $t_{*,100}$ corresponds to the “envelope infall” stage

⁵ In reality, the accretion after t_{coll} would be affected by winds and radiation from a protostellar system, which are not included in our simulations.

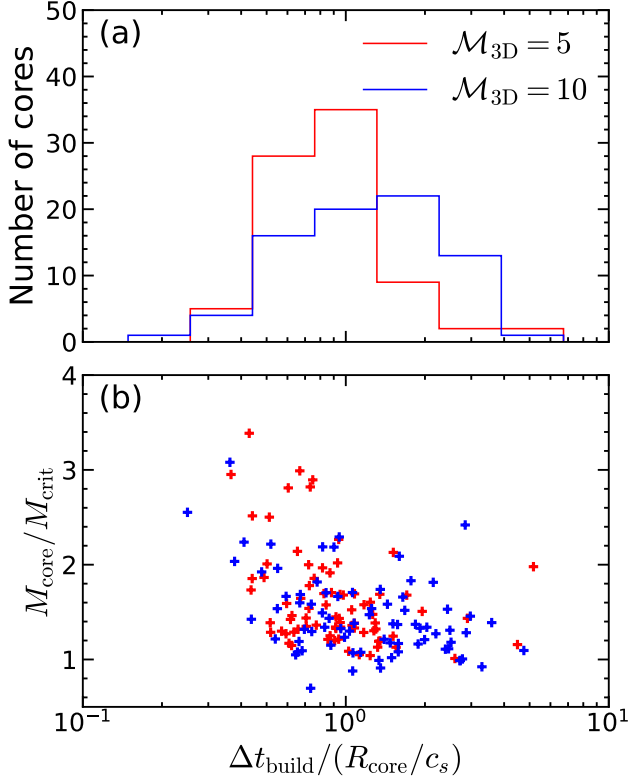


Figure 11. (a) The distribution of the ratio between the core building time (Equation (38)) and the sound crossing time for model M5 (red) and M10 (blue). (b) The ratio between the core mass to the critical mass versus the normalized core building time. The critical mass is calculated using Equation (10) with the measured average density $\bar{\rho}$ and velocity dispersion σ_{1D} of each critical core. The median ratio is $M_{\text{core}}/M_{\text{crit}} = 1.6$ and 1.3 for the range $\Delta t_{\text{build}}/(R_{\text{core}}/c_s) < 1$ and > 1 , respectively.

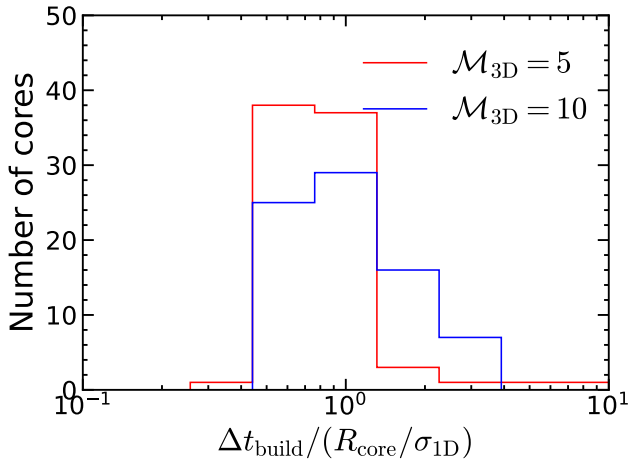


Figure 12. Similar to Figure 11(a), but for the building time normalized to the turbulent crossing time $R_{\text{core}}/\sigma_{1D}$.

of Gong & Ostriker (2009), for which we define

$$\Delta t_{\text{infall}} \equiv t_{*,100} - t_{\text{coll}}. \quad (41)$$

Figure 10(c) shows that Δt_{infall} is typically shorter than the free-fall time associated with the mean core density $\bar{\rho}_{\text{coll}}$ at the end of the collapse⁶, with the median at $\Delta t_{\text{infall}} = 0.6 t_{\text{ff}}(\bar{\rho}_{\text{coll}})$. This is not surprising considering that by the time t_{coll} , the core inflow has already achieved supersonic velocities (see Figure 11 in Paper II) such that it takes less time to reach the center compared to the free-fall from initially at rest. We note that Gong & Ostriker (2009, Figure 12) found $\Delta t_{\text{infall}}/t_{\text{ff}}(\bar{\rho}_{\text{coll}}) \sim 0.8\text{--}1$ in their one-dimensional converging flow simulations.

Figure 9(b) shows that the sink mass continues to grow even after $t_{*,100}$ without noticeable decline in the accretion rate. As previously pointed out by Gong & Ostriker (2015, see their Figure 20), this late accretion (in the terminology of Gong & Ostriker 2009) is expected since cores are not isolated objects truncated at a finite radius, but instead are the inner parts of converging flows that continue to be accreted onto the sink particle. For example, Figure 9(d) indicates that the time-averaged inflow rate at $r = R_{\text{core}}$ during the envelope infall stage is about a half as large as the sink particle accretion rate during the same time period.

In reality, however, the accreting flows likely arrive at a protostellar disk rather than directly onto the forming protostar, such that only a fraction of $\dot{M}_{\text{in}}(r \rightarrow 0)$ would ultimately reach the protostellar surface. In addition, radiation and/or bipolar outflows from the forming protostar would limit the accretion rate during the envelope infall and late accretion stages for some systems (e.g., Hansen et al. 2012; Kuiper et al. 2016). However, the persistence of accretion after the initial core is consumed may be essential for the formation of massive stars. Based on our simulations, it does not appear possible for massive stars to originate as massive, highly turbulent, quasi-equilibrium cores that become supercritical and collapse. An alternative would be sustained accretion from a larger-scale converging flow.

Finally, Figure 10(d) compares Δt_{build} , Δt_{coll} , and Δt_{infall} on a common scale, showing that the characteristic timescales becoming shorter and shorter as a core evolves to later stages. The median value for each stages are $\Delta t_{\text{build}} \sim 0.19 t_{\text{ff},0}$, $\Delta t_{\text{coll}} \sim 0.086 t_{\text{ff},0}$, and

⁶ As the collapse proceeds the mean density within the “Lagrangian radius” r_M enclosing M_{core} increases such that $\bar{\rho}_{\text{coll}} \equiv M_{\text{core}}/(4\pi r_M^3/3) \sim 3\bar{\rho}_{\text{crit}}$, where $\bar{\rho}_{\text{crit}} \equiv M_{\text{core}}/(4\pi R_{\text{core}}^3/3)$. The free-fall time correspondingly decreases to $t_{\text{ff}}(\bar{\rho}_{\text{coll}}) \sim 0.6 t_{\text{ff}}(\bar{\rho}_{\text{crit}})$.

$\Delta t_{\text{infall}} \sim 0.031 t_{\text{ff},0}$, where $t_{\text{ff},0} \sim 3\text{--}6$ Myr under typical GMC conditions (Equation (19)).

5. DISCUSSION

5.1. Is There a Threshold Density?

A recurring theme in star formation theory is that there exists a “threshold density” above which gas is gravitationally unstable. For example, based on different physical arguments and assumptions, Krumholz & McKee (2005) and Padoan & Nordlund (2011) proposed that there exists a threshold density above which a core becomes unstable and collapses. For a spherical cloud with the virial parameter $\alpha_{\text{vir}} = 5\sigma_{1\text{D}}^2 R_{\text{cloud}} / (GM_{\text{cloud}})$ and Mach number $\mathcal{M}_{3\text{D}} = \sqrt{3}\sigma_{1\text{D}}/c_s$, the threshold density (relative to the mean cloud value ρ_0) predicted from these theories is $\rho_{\text{thr}}/\rho_0 = (0.28\text{--}0.55) \times \alpha_{\text{vir}} \mathcal{M}_{3\text{D}}^2$ (the smaller and larger coefficients correspond to the theory of Krumholz & McKee 2005 and Padoan & Nordlund 2011, respectively, with their fiducial choice of order-unity parameters; we assume $p = 0.5$ for the former theory).

When applied to our models by taking $M_{\text{cloud}} = M_{\text{box}}$ and $4\pi R_{\text{cloud}}^3/3 = L_{\text{box}}^3$ leading to $\alpha_{\text{vir}} \approx 2$, the theories of Krumholz & McKee (2005) and Padoan & Nordlund (2011) predicts that the threshold density lies somewhere in between $\rho_{\text{thr}}/\rho_0 = 14\text{--}28$ and $56\text{--}110$ for models M5 and M10, respectively. Although the measured distributions of critical core mean density (Figure 5(c)) start to rise roughly around the predicted range of ρ_{thr} , the distribution extends widely above and below ρ_{thr} . This indicates that the threshold density of Krumholz & McKee (2005) or Padoan & Nordlund (2011) is neither a necessary nor sufficient condition for collapse of individual cores. Figure 5(a) also shows a broad range of central density at the critical time. Indeed, Figure 3 indicates that individual cores start to collapse at a wide range of densities, due both to the spatially varying strength of turbulence (Figure 2(a)), and to the varying tidal environment in which they are born.

Rather than a single threshold density, there may be a characteristic density set by the global parameters of a cloud, with more specific critical criteria responsive to local variations in conditions. We note that very different physical arguments lead to similar characteristic densities of gravitationally unstable cores. For example, considerations of anisotropic core formation mediated by magnetic fields in local converging flows lead to $\rho_{\text{char}}/\rho_0 = 0.56\mathcal{M}_{3\text{D}}^2$ for $\mathcal{M}_{3\text{D}}$ the flow Mach number (Chen & Ostriker 2015, from Eqn. (6) and (7); see also Chen & Ostriker 2014). For $\alpha_{\text{vir}} \sim 2$, all these characteristic densities are comparable to a simple “post-shock”

density $\mathcal{M}_{3\text{D}}^2 \rho_0$ multiplied by some order unity coefficient.

The TES model provides a more mathematical route to a characteristic unstable-core density based on cloud-scale parameters, yielding a similar value to characteristic densities obtained from various physical arguments described above. Combining Equation (14) with Equation (12) (assuming $p = 0.5$ and $\eta_d = 0.9$) and Equation (21), the average density of critical cores forming in a spherical cloud under “typical” turbulence conditions (i.e., $r_s \sim r_{s,\text{cloud}} = (9/4)(R_{\text{cloud}}/\mathcal{M}_{3\text{D}}^2)$) is

$$\frac{\rho_{\text{char}}}{\rho_0} = 0.11 \frac{\left[1 + \frac{1}{2} \left(\frac{\sigma_{1\text{D}}}{c_s}\right)^2\right]^{2/3}}{\left(\frac{\sigma_{1\text{D}}}{c_s}\right)^4} \alpha_{\text{vir}} \mathcal{M}_{3\text{D}}^2 \quad (42)$$

$$\sim 0.3 \alpha_{\text{vir}} \mathcal{M}_{3\text{D}}^2,$$

where we take $\sigma_{1\text{D}} = 0.8c_s$ as a representative value (e.g., Figure 4(d)) in the second equality. For a cloud with $\alpha_{\text{vir}} \sim 2\text{--}4$, Equation (42) says that ρ_{char} is essentially the post-shock density, $\mathcal{M}_{3\text{D}}^2 \rho_0$, for an isothermal shock.

Of course, in order for collapse to occur, the core radius – which depends on the local tidal gravitational field – must exceed the critical radius. If we use the above ρ_{char} in Equation (9) and Equation (10), adopting $\sigma_{1\text{D}}/c_s = 0.8$ as before, we find a characteristic radius and mass for critical cores of $R_{\text{char}} = 0.83 L_{\text{J},0} / (\alpha_{\text{vir}}^{1/2} \mathcal{M}_{3\text{D}})$ (comparable to the mean sonic radius in the cloud, from Equation (21)) and $M_{\text{char}} = 0.78 M_{\text{J},0} / (\alpha_{\text{vir}}^{1/2} \mathcal{M}_{3\text{D}})$, where Equation (16) and Equation (17) can be used to convert to physical units. For typical GMC parameters, $R_{\text{char}} \sim 0.08$ pc and $M_{\text{char}} \sim 1.8 M_{\odot}$.

When considering the effects of turbulence, almost all theories assume that a single linewidth–size relation applies to all cores and that the turbulent velocities are completely independent of the density. However, Figure 2(a) (see also Figure 15 of Paper II) shows that both the slope and normalization of the *local* linewidth–size relations significantly vary from region to region. While we took $r_s = r_{s,\text{cloud}}$ and $p = 0.5$ in deriving Equation (42), in reality, these local variations in the turbulent scaling relations would modify the leading numerical coefficient in Equation (42) proportional to $(r_s/r_{s,\text{cloud}})^{-2} \propto (\sigma_{1\text{D}}/c_s)^4$, in addition to the variation in $\sigma_{1\text{D}}/c_s$ of the square bracketed factors. This would lead to a range of critical densities at which collapse is triggered, as is seen in our distributions in Figure 5 (see also Figure 3). A more refined theory should therefore draw the turbulent velocity dispersion (or the local sonic scale) from a joint distribution of density and velocity

dispersion rather than assuming a single linewidth–size relation independent of density.

To summarize, Equation (42) implies that the variation in the characteristic density ρ_{char} reflects differences in global physical conditions — ρ_0 , α_{vir} , and $\mathcal{M}_{3\text{D}}$ — across star forming regions. In addition to this, within a single cloud, correlated variations between local density and turbulence result in a distribution of critical densities around ρ_{char} (see Figure 2).

5.2. Absence of highly-turbulent cores

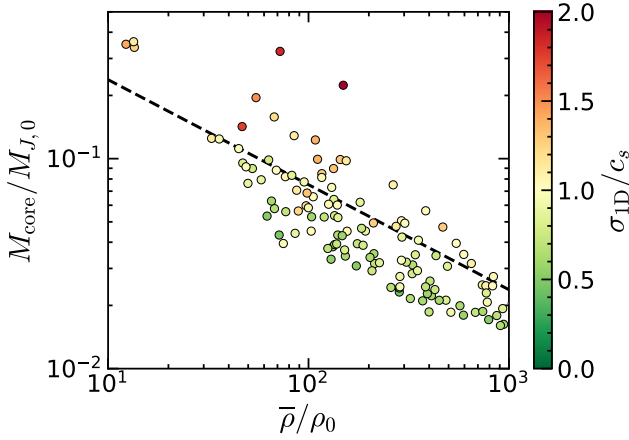


Figure 13. Core mass versus mean core density for the critical cores in model M10 satisfying $r_{\text{crit}} \geq 4\Delta x$ (i.e., $N_{\text{core, res}} = 4$), color coded by their internal velocity dispersion. Dashed line plots $M_{\text{core}} = 1.5M_{\text{crit}}$ for M_{crit} as given in Equation (10) adopting $\sigma_{1\text{D}} = c_s$, with the factor 1.5 the typical mass excess found in our simulations (Figure 11(b)). As predicted in Equation (10), core mass also increases with core velocity dispersion (green to red).

Our simulations show that the vast majority (96%) of the critical cores that are the immediate precursors of star formation have radial turbulent velocity dispersion $\sigma_{1\text{D}} < 1.5c_s$, and even the most turbulent critical core has $\sigma_{1\text{D}} = 2.1c_s$. That is, the turbulence is at most trans-sonic. It is worth emphasizing that this lack of highly turbulent critical cores was not a foregone conclusion. Indeed, the total mass $M_{\text{box}} = 64M_{J,0}$ and turbulent velocity dispersion $\mathcal{M}_{3\text{D}} = 10$ in model M10 are large enough such that supersonically turbulent cores with $\sigma_{1\text{D}}/c_s \gtrsim 3$ could have formed. For example, setting $\sigma_{1\text{D}}/c_s = 5$ in Equation (10) yields $M_{\text{crit}} = 4.5(\bar{\rho}/\rho_0)^{-1/2}M_{J,0} \ll M_{\text{box}}$ for mean core density $\bar{\rho}$. Our results therefore suggest that, although the TES theory and the initial condition of our numerical models permit the existence of highly turbulent cores, they are not easily realized in the actual outcome. Equation (10) suggests that core mass is inversely correlated

with local density and positively correlated with local velocity dispersion, and our numerical results are consistent with this (see Figure 13). However, we find only a limited range of core velocity dispersion.

In terms of mass, the CCMF above the peak in our simulations is well fit by a lognormal function with the standard deviation 0.55, consistent with the Chabrier IMF. It is notable also that (1) from Figure 4(d), all of the cores have relatively low internal turbulence levels (the distribution of $\sigma_{1\text{D}}/c_s$ peaks at a subsonic level), and (2) the most massive cores in our simulations are not highly-turbulent cores, but rather those forming in lower density environments. Purely hypothetically, our simulations could have produced quite different outcomes. For example, only a few highly turbulent, very massive cores could have been produced. The CCMF in such a hypothetical scenario would be very different from what we actually found and present in this paper, in terms of the peak position and the width of the distribution. Taken together, we do not find evidence supporting the McKee & Tan (2003) theory (see also Myers & Fuller 1992; McLaughlin & Pudritz 1997), in which the precursors of massive stars are massive cores supported by high-amplitude turbulence, although we cannot completely rule out the possible existence of such massive turbulent cores given our limited statistics and box-scale Mach number.

From a physical point of view, the idea of massive cores supported primarily by turbulence suffers from two main difficulties. One is that highly supersonic turbulence would produce a high degree of substructure, so that even if a core has strong enough gravity to collapse, it would rapidly fragment rather than producing a single massive star. The second is that strong turbulence implies a flow crossing time comparable to the gravitational timescale, so that highly turbulent structures are also highly transient. For critical TESs, the ratio of the turbulent crossing time $\Delta t_{\text{cross}} \equiv R_{\text{core}}/\sigma_{1\text{D}}$ to the free-fall time at average density decreases from $\Delta t_{\text{cross}}/t_{\text{ff}} = 1.6$ at $\sigma_{1\text{D}}/c_s = 1$ to $\Delta t_{\text{cross}}/t_{\text{ff}} = 0.82$ at $\sigma_{1\text{D}}/c_s = 3$ (see also Figure 8(d) of Paper I). Figure 12 indicates that on average the median core building time is shorter than the turbulent crossing time, and that less than 10% of cores have $\Delta t_{\text{build}}/\Delta t_{\text{cross}} > 2$. This suggests that massive, turbulently supported cores would self-destruct before they succeed in assembling enough mass to become unstable.

Recent high-resolution observations also do not find strong evidence of high-mass, highly turbulent prestellar cores (e.g., Sanhueza et al. 2019; Redaelli et al. 2022; Li et al. 2023; Morii et al. 2023; Nony et al. 2023); often, previous high-mass prestellar core candidates turn

out to be protostellar in nature or resolved into a collection of lower-mass substructures when resolution is increased. Observed *protostellar* cores in high-mass star-forming regions are on average more massive than prestellar cores and have shallower CMF slope (Li et al. 2023; Nony et al. 2023), suggesting cores continue to grow in mass after collapse. Taken together, the lack of highly turbulent, massive prestellar cores and the presence of continued accretion well beyond the time of collapse (e.g., Figure 9) support the idea that massive stars form by accretion flows from scales beyond the critical core (see Section 2.6.2 of Motte et al. 2018 for a review; see also Padoan et al. 2020), rather than by collapse of highly turbulent, massive prestellar cores.

5.3. The CMF in Numerical Simulations

Various theoretical arguments suggest that as a result of supersonic turbulence, the CMF defined by the number of cores per logarithmic mass bin has peak at a characteristic mass scale set by the large-scale physical conditions in the cloud (e.g., Equations (34) and (35), Gong & Ostriker 2011; Chen & Ostriker 2014, 2015; Haugbølle et al. 2018; see also Padoan & Nordlund 2002; Hennebelle & Chabrier 2008; Hopkins 2012 for related theories that make predictions for the whole CMF). Even if the full CMF does not directly map to the stellar initial mass function (IMF) due to late-stage accretion and disk fragmentation, a peak in the CMF could potentially have implications for the turnover of the IMF or the mass function of stellar systems, allowing for fragmentation into a binary or multiple at a later evolutionary stage (see e.g. review by Offner et al. 2023).

It has been questioned in the literature, however, whether cloud-scale conditions (including an effectively isothermal equation of state, given the balance of heating and cooling) and the physics of self-gravitating turbulence are ever able to imprint a characteristic mass scale, and if so, whether this is relevant to the IMF (e.g., Martel et al. 2006; Federrath et al. 2017; Guszejnov et al. 2018, 2020, see also Section 5 of Hennebelle & Grudić 2024 for a recent review). Regarding the first question, it has been suggested that non-convergence of mass functions is a general feature of self-gravitating, isothermal numerical simulations. For example, Guszejnov et al. (2018) found no convergence with increasing numerical resolution in the low-mass spectrum of the SMF for their isothermal, unmagnetized self-gravitating turbulence simulations, and Guszejnov et al. (2020, see their Figure 10) found lack of convergence in the low mass end of the SMF in their isothermal magnetohydrodynamic (MHD) simulations. Although their specific results regarding lack of low-mass convergence may have

been compromised by an error in their sink particle implementation (see Guszejnov et al. 2021), a more general issue is that this approach does not distinguish between convergence in the CMF and convergence in the SMF.

Indeed, when discussing numerical convergence of mass functions, most studies have presented results based on the SMF rather than the CMF (e.g., Martel et al. 2006; Federrath et al. 2017; Guszejnov et al. 2018; Lee & Hennebelle 2018; Haugbølle et al. 2018; see, however, Chen & Ostriker 2014, 2015; Gong & Ostriker 2015; Padoan et al. 2020; Pelkonen et al. 2021 for the CMF). While the CMF in observations reflects cloud-scale dynamics and choices in segmentation algorithms, and the CCMF studied in the present work focuses on the initial conditions for formation of star-disk systems, additional effects (both physical and numerical) enter in determining the SMF in simulations, so that one does not necessarily map to the other. Collapsing cores or disks may fragment (although the fragmentation *during* core collapse may be difficult; see Tohline 1980a,b; Hanawa & Matsumoto 1999; Lai 2000; Sugimura et al. 2017), and cores that collapse may continue to accrete, growing in mass (as shown by Figure 9; see also Padoan et al. 2020; Pelkonen et al. 2021). The SMF measured at any given moment will include young sink particles that have accreted only a small fraction of the parental core mass, as well as old sink particles that become overmassive through sustained accretion if realistic feedback is not included. Additionally, the SMF may include spurious sink particles formed in unresolved cores that would otherwise have been torn apart by turbulence at higher resolution, and low-mass sinks forming within disks around sink particles at late stages of evolution. Disk fragmentation is subject to tidal forces and heating once a central protostar has formed (see Kratter & Lodato 2016, for a review), and while these effects are important in setting the IMF they are not relevant to the cloud-scale gravo-turbulent fragmentation process. The SMF can also be affected by the choice of subgrid model parameters, as shown by Haugbølle et al. (2018, Appendix C). Thus, in order to properly distinguish the roles of gravo-turbulent fragmentation on cloud scales from disk-scale fragmentation, we strongly encourage measuring and studying CMFs in numerical simulations. Although there is no single “correct” definition of a prestellar core, the criteria we have developed based on the theoretical critical radius compared to the tidal radius (and transition from positive to negative net force) provide physically motivated definitions, which leads to the CCMF in this work. Following the full history prior to, during, and subsequent to collapse would be necessary to

test theories of the CMF and to understand the relation between the CMF and the IMF.

To claim the existence or absence of a numerically converged mass function (whether it is the CMF or the SMF), it is necessary to achieve numerical resolution high enough to unambiguously resolve the anticipated characteristic mass. In [Appendix A](#), we intercompare various measures of numerical resolution in recent self-gravitating turbulence simulations, which is relevant to the question of numerical convergence in mass functions.

5.4. Connection to Observations

Because a primary goal in this work was to test the applicability of the semianalytic TES model, the simulations presented in [Paper II](#) and in this work are highly idealized by construction. Furthermore, the physical properties of cores are measured at a very particular epoch, t_{crit} , corresponding to the onset of runaway collapse for each core. While it is therefore premature to attempt comprehensive comparisons to observed core properties, it is worthwhile noting a few key points. Taking the reference values for the temperature and ambient density in [Equations \(16\) and \(17\)](#), the typical mass and radius of the critical cores ([Figure 6](#)) are, in physical units, $\sim 2 M_{\odot}$ and ~ 0.1 pc, respectively, which are similar to the upper envelope of the observed starless/prestellar core distribution from Herschel/JCMT Gould Belt Surveys ([Kirk et al. 2013; Könyves et al. 2015; Pattle et al. 2015; Salji et al. 2015; Kirk et al. 2016; Ward-Thompson et al. 2016; Mowat et al. 2017; Pattle et al. 2017; Benedettini et al. 2018; Bresnahan et al. 2018; Di Francesco et al. 2020; Könyves et al. 2020; Fiorellino et al. 2021; Pezzuto et al. 2021; Kirk et al. 2024; Pattle et al. 2025](#)). We note that the critical core properties are taken at the onset of collapse; as the cores subsequently evolve to higher central column densities, their “observational radius” based on the column density FWHM would decrease over time. The observed core radius also depends on adopted definitions and details of background subtraction procedure. Hence, care must be taken to uniformly compare the observed and simulated core sample.

Observations generally report outer density profiles that are shallower than r^{-2} but steeper than r^{-1} ([Bergin & Tafalla 2007; di Francesco et al. 2007; Chen et al. 2019](#)). This is similar to the theoretical prediction from the TES model ([Paper I](#), see [Figures 6 and 7](#) there) and to the density profiles of critical cores shown here ([Figure 1](#)). Consistent with our findings for the critical cores in our simulations, spectral line surveys find that the average line widths of cores are largely transonic ([Lee et al. 1999, 2001; Foster et al. 2009; Friesen](#)

[et al. 2009, 2010; Lee et al. 2014; Storm et al. 2016; Keown et al. 2017; Kirk et al. 2017; Tang et al. 2018; Chen et al. 2019; Chung et al. 2019; Kerr et al. 2019; Choudhury et al. 2021; Chung et al. 2021; Li et al. 2023; Yoo et al. 2023](#)).

We also note that $M_{\text{core}} \propto \bar{\rho}^{-1/2}$ relation evident in [Figure 13](#) suggests that the mass of critical cores is overall proportional to their size. In fact, combination of [Equations \(1\), \(2\), \(9\) and \(10\)](#) gives a mass-size relation for the critical TES:

$$M_{\text{crit}} = 2.44 \frac{c_s^2}{G} r_{\text{crit}} \left(1 + \frac{1}{2} \frac{\sigma_{1D}^2}{c_s^2} \right)^{2/3}; \quad (43)$$

for a limited range of σ_{1D}/c_s this would indeed represent a roughly linear relationship. In principle, [Equation \(43\)](#) is of value when interpreting the observed mass–size relations of starless cores (e.g., [Kirk et al. 2013; Könyves et al. 2015; Pattle et al. 2015; Salji et al. 2015; Kirk et al. 2016; Ward-Thompson et al. 2016; Keown et al. 2017; Kirk et al. 2017; Mowat et al. 2017; Pattle et al. 2017; Benedettini et al. 2018; Bresnahan et al. 2018; Chen et al. 2019; Di Francesco et al. 2020; Könyves et al. 2020; Fiorellino et al. 2021; Pezzuto et al. 2021; Kirk et al. 2024](#)). However, a direct comparison may be difficult, because observed cores are at various evolutionary stages (as opposed to at t_{crit} ; see however [Simpson et al. 2011](#) and [Bresnahan et al. 2018](#) for evolutionary modeling), and widely different methods are empirically adopted for defining core boundaries (and background subtracting), which affect both the mass and the size.

As already discussed in [Section 6.2 of Paper I](#), it will be very interesting to examine how projection effects map the intrinsic power-law structure function found within the critical cores ([Figure 2\(a\)](#)) to the observed linewidth–size relation. Our preliminary analysis ([Moon & Ostriker, in prep.](#)) indicates that, even though the intrinsic turbulent velocity dispersion grows in radius as a power law within cores, the line-of-sight velocity dispersion flattens toward the center in the sky plane due to density-weighted projection effects (see also [Section 3.1.2 of McKee & Ostriker 2007](#)). This implies that observed “coherent cores,” which have roughly constant non-thermal velocity dispersion profiles and shallower-than-BE density profiles (e.g., [Goodman et al. 1998; Pineda et al. 2010; Chen et al. 2019](#)) might be partly supported by turbulence, and evolving toward the onset of collapse.

6. SUMMARY AND CONCLUSIONS

Prestellar cores form within turbulent GMCs and undergo gravitational runaway at some point in their life, leading to star formation. To understand the physical

processes responsible for triggering collapse, it is essential to investigate the detailed evolution of individual cores and their physical properties at the onset of collapse. In the companion paper (Paper II), we have conducted a comprehensive analysis of the evolution of individual cores, using a carefully constructed suite of numerical simulations of turbulent, self-gravitating clouds. In this work, we investigate the structure and physical properties of these cores measured at the *critical time* when they initiate collapse (Section 3), and interpret these results using our new model for TESs developed in Paper I. We also measure the inflow rates before and after the collapse, which determine the timescales the cores spend in each evolutionary stage (Section 4).

Our main conclusions are as follows:

1. Within cores, the turbulent velocity dispersion increases with distance r approximately as a power-law (Figure 2(a)), validating the main assumption of the TES model developed in Paper I. The measured angle-averaged radial density profiles are close to the theoretical prediction of the TES model for both quiescent and highly turbulent cores (Figure 1), even though the majority of cores are triaxial with mean axis ratios of 0.73 and 0.45 (Figure 8). The BE sphere profile is too steep to explain the density structure of turbulent cores.
2. The cores in our simulations have subsonic or transonic internal velocity dispersions ($\sigma_{1D} \sim 0.5\text{--}1.5c_s$) at the onset of the collapse (Figure 4(d)), consistent with observed superthermal linewidths (e.g., Lee et al. 1999, 2001; Foster et al. 2009; Friesen et al. 2009, 2010; Lee et al. 2014; Storm et al. 2016; Keown et al. 2017; Kirk et al. 2017; Tang et al. 2018; Chen et al. 2019; Chung et al. 2019; Kerr et al. 2019; Choudhury et al. 2021; Chung et al. 2021; Li et al. 2023; Yoo et al. 2023). The slope of the internal linewidth–size relation of cores is $p \sim 0.5 \pm 0.2$ (Figure 4(a)), similar to the slope of the linewidth–size relation on large scales in our simulations (and observed GMCs). We do not find evidence for highly turbulent, massive prestellar cores (see Section 5.2 for related discussion). However, we do find evidence for continued accretion beyond the core collapse (Figure 9(b)), which may be responsible for the formation of massive stars.
3. The building, collapse, and infall stages of core evolution have successively shorter durations (Figure 10), decreasing from a median of 0.19 to 0.086 to 0.031 times the free-fall time $t_{ff,0}$ at the mean density of the surrounding cloud. This implies

that observed timescales would become shorter as cores evolve from prestellar to protostellar phases. Since the mean core densities are ~ 100 times average cloud values, the duration of prestellar evolutionary stages is ~ 3 times the internal free-fall time within the critical cores. Core building takes only a single sound crossing time (Figure 11), indicating that cores form rapidly by dynamical compression rather than quasi-static processes. The prolonged collapse duration relative to the central free-fall time, $\Delta t_{\text{coll}} \sim 2t_{\text{ff,c}}$, is consistent with the small net force applied throughout the collapse (Paper II).

4. Cores form at a wide range of densities (Figure 5), with most having a center-to-edge density contrast of $\sim 10\text{--}30$ (here, “edge” means $r = r_{\text{crit}}$), consistent with theoretical expectations based on the TES model in Paper I with at most transonic internal turbulence. The distribution of ratios of the core internal density to the mean cloud density on large scales peaks at $\bar{\rho}/\rho_0 \sim 100$ for both our M5 and M10 models (although the peak would likely shift to higher densities for model M10 when resolution is increased), extending down to ~ 10 for M10, and lower for M5. There is no sign of a single threshold density for collapse, as has been proposed in some theories for determining the star formation rate in molecular clouds. Local variations in the turbulence strength are significant even within a single cloud, affecting the density at which cores become unstable (Figures 2 and 3). The distribution of critical core densities is directly related to the CMF, which shows marginal evidence of a peak consistent with a characteristic post-shock critical mass $M_{\text{char, trb}}$ associated with the initial cloud-scale Mach number (Figure 6(a)). Resolving the peak of the CMF requires the minimum resolvable mass far smaller than the characteristic mass, which becomes increasingly challenging for higher Mach number (Appendix A).
5. Prestellar cores – i.e. the immediate precursors of stars, as measured at t_{crit} – have distinctive structural and dynamic properties, marking this as a key stage of star formation. However, our analysis implies that the CMF does not map directly to the IMF, at least on the high-mass end. In particular, we do not find evidence for massive prestellar cores supported by turbulence. Instead, given that the mass accretion rate measured at a fixed radius, $\dot{M}_{\text{in}}(r = R_{\text{core}})$ stays roughly constant or even slightly increases both before and

after the collapse (Figure 9(a)), our results suggest that more massive stars may form due to sustained accretion. After the sink particle forms, its accretion rate (which in a real system would be the onto a circumstellar disk) remains at a steady level $\sim (10\text{--}20)c_s^3/G$ (Figure 9(b),(d)), comparable to $\dot{M}_{\text{in}}(r = R_{\text{core}})$.

As noted in Paper II, a limitation of the present set of simulations is the absence of magnetic fields. It will be very interesting to consider models with varying magnetic field strength, in order to test whether the properties of critical cores end up being consistent with the anisotropic model outlined in Chen & Ostriker (2014, 2015), in the sense of evolving to become magnetically supercritical by inflow along magnetic fields (reaching $v_A \sim c_s$), while simultaneously also having similar turbulence properties (with $\sigma_{1D} \sim c_s$) to cores in the present simulations.

Another caveat is the omission of protostellar feedback in our simulations. The injection of energy and momentum via radiation and outflows can play a signifi-

cant role in regulating accretion onto nascent protostars. Properly modeling these processes is therefore crucial for understanding the full star formation process. The injected momentum can also locally perturb the velocity field within nearby prestellar cores (e.g., Verliat et al. 2022; Neralwar et al. 2024), although protostellar outflows are usually highly collimated such that substantial fraction of core-forming dense gas could remain intact (Hansen et al. 2012; see also Frank et al. 2014; Bally 2016 for a review). In the future, it might be interesting to compare the sonic radius distribution of critical cores with and without outflow feedback included.

ACKNOWLEDGMENTS

We thank the anonymous referee for constructive comments which greatly improved the quality of this paper. This work was supported in part by grant 510940 from the Simons Foundation to E. C. Ostriker. Computational resources for this project were provided by Princeton Research Computing, a consortium including PICSciE and OIT at Princeton University.

REFERENCES

- André, P., Di Francesco, J., Ward-Thompson, D., et al. 2014, in *Protostars and Planets VI*, ed. H. Beuther, R. S. Klessen, C. P. Dullemond, & T. Henning, 27–51, doi: [10.2458/azu_uapress_9780816531240-ch002](https://doi.org/10.2458/azu_uapress_9780816531240-ch002)
- Andre, P., Ward-Thompson, D., & Barsony, M. 2000, in *Protostars and Planets IV*, ed. V. Mannings, A. P. Boss, & S. S. Russell, 59, doi: [10.48550/arXiv.astro-ph/9903284](https://doi.org/10.48550/arXiv.astro-ph/9903284)
- Bally, J. 2016, *ARA&A*, 54, 491, doi: [10.1146/annurev-astro-081915-023341](https://doi.org/10.1146/annurev-astro-081915-023341)
- Basu, S., & Ciolek, G. E. 2004, *ApJL*, 607, L39, doi: [10.1086/421464](https://doi.org/10.1086/421464)
- Benedettini, M., Pezzuto, S., Schisano, E., et al. 2018, *A&A*, 619, A52, doi: [10.1051/0004-6361/201833364](https://doi.org/10.1051/0004-6361/201833364)
- Bergin, E. A., & Tafalla, M. 2007, *ARA&A*, 45, 339, doi: [10.1146/annurev.astro.45.071206.100404](https://doi.org/10.1146/annurev.astro.45.071206.100404)
- Bonnor, W. B. 1956, *MNRAS*, 116, 351, doi: [10.1093/mnras/116.3.351](https://doi.org/10.1093/mnras/116.3.351)
- Bresnahan, D., Ward-Thompson, D., Kirk, J. M., et al. 2018, *A&A*, 615, A125, doi: [10.1051/0004-6361/201730515](https://doi.org/10.1051/0004-6361/201730515)
- Chen, C.-Y., & Ostriker, E. C. 2014, *ApJ*, 785, 69, doi: [10.1088/0004-637X/785/1/69](https://doi.org/10.1088/0004-637X/785/1/69)
- . 2015, *ApJ*, 810, 126, doi: [10.1088/0004-637X/810/2/126](https://doi.org/10.1088/0004-637X/810/2/126)
- . 2018, *ApJ*, 865, 34, doi: [10.3847/1538-4357/aad905](https://doi.org/10.3847/1538-4357/aad905)
- Chen, H. H.-H., Pineda, J. E., Goodman, A. A., et al. 2019, *ApJ*, 877, 93, doi: [10.3847/1538-4357/ab1a40](https://doi.org/10.3847/1538-4357/ab1a40)
- Choudhury, S., Pineda, J. E., Caselli, P., et al. 2021, *A&A*, 648, A114, doi: [10.1051/0004-6361/202039897](https://doi.org/10.1051/0004-6361/202039897)
- Chung, E. J., Lee, C. W., Kim, S., et al. 2019, *ApJ*, 877, 114, doi: [10.3847/1538-4357/ab12d1](https://doi.org/10.3847/1538-4357/ab12d1)
- . 2021, *ApJ*, 919, 3, doi: [10.3847/1538-4357/ac0881](https://doi.org/10.3847/1538-4357/ac0881)
- Collins, D. C., Le, D. K., & Jimenez Vela, L. L. 2024, *MNRAS*, 532, 681, doi: [10.1093/mnras/stae1493](https://doi.org/10.1093/mnras/stae1493)
- di Francesco, J., Evans, N. J., I., Caselli, P., et al. 2007, in *Protostars and Planets V*, ed. B. Reipurth, D. Jewitt, & K. Keil, 17, doi: [10.48550/arXiv.astro-ph/0602379](https://doi.org/10.48550/arXiv.astro-ph/0602379)
- Di Francesco, J., Keown, J., Fallscheer, C., et al. 2020, *ApJ*, 904, 172, doi: [10.3847/1538-4357/abc016](https://doi.org/10.3847/1538-4357/abc016)
- Ebert, R. 1955, *ZA*, 37, 217
- . 1957, *ZA*, 42, 263
- Federrath, C., Krumholz, M., & Hopkins, P. F. 2017, in *Journal of Physics Conference Series*, Vol. 837, *Journal of Physics Conference Series (IOP)*, 012007, doi: [10.1088/1742-6596/837/1/012007](https://doi.org/10.1088/1742-6596/837/1/012007)
- Fiorellino, E., Elia, D., André, P., et al. 2021, *MNRAS*, 500, 4257, doi: [10.1093/mnras/staa3420](https://doi.org/10.1093/mnras/staa3420)
- Foster, J. B., Rosolowsky, E. W., Kauffmann, J., et al. 2009, *ApJ*, 696, 298, doi: [10.1088/0004-637X/696/1/298](https://doi.org/10.1088/0004-637X/696/1/298)

- Foster, P. N., & Chevalier, R. A. 1993, *ApJ*, 416, 303, doi: [10.1086/173236](https://doi.org/10.1086/173236)
- Frank, A., Ray, T. P., Cabrit, S., et al. 2014, in *Protostars and Planets VI*, ed. H. Beuther, R. S. Klessen, C. P. Dullemond, & T. Henning, 451–474, doi: [10.2458/azu-uapress.9780816531240-ch020](https://doi.org/10.2458/azu-uapress.9780816531240-ch020)
- Friesen, R. K., Di Francesco, J., Shimajiri, Y., & Takakuwa, S. 2010, *ApJ*, 708, 1002, doi: [10.1088/0004-637X/708/2/1002](https://doi.org/10.1088/0004-637X/708/2/1002)
- Friesen, R. K., Di Francesco, J., Shirley, Y. L., & Myers, P. C. 2009, *ApJ*, 697, 1457, doi: [10.1088/0004-637X/697/2/1457](https://doi.org/10.1088/0004-637X/697/2/1457)
- Gammie, C. F., Lin, Y.-T., Stone, J. M., & Ostriker, E. C. 2003, *ApJ*, 592, 203, doi: [10.1086/375635](https://doi.org/10.1086/375635)
- Gong, H., & Ostriker, E. C. 2009, *ApJ*, 699, 230, doi: [10.1088/0004-637X/699/1/230](https://doi.org/10.1088/0004-637X/699/1/230)
- . 2011, *ApJ*, 729, 120, doi: [10.1088/0004-637X/729/2/120](https://doi.org/10.1088/0004-637X/729/2/120)
- Gong, M., & Ostriker, E. C. 2015, *ApJ*, 806, 31, doi: [10.1088/0004-637X/806/1/31](https://doi.org/10.1088/0004-637X/806/1/31)
- Goodman, A. A., Barranco, J. A., Wilner, D. J., & Heyer, M. H. 1998, *ApJ*, 504, 223, doi: [10.1086/306045](https://doi.org/10.1086/306045)
- Guszejnov, D., Grudić, M. Y., Hopkins, P. F., Offner, S. S. R., & Faucher-Giguère, C.-A. 2020, *MNRAS*, 496, 5072, doi: [10.1093/mnras/staa1883](https://doi.org/10.1093/mnras/staa1883)
- . 2021, *MNRAS*, 500, 1125, doi: [10.1093/mnras/staa3413](https://doi.org/10.1093/mnras/staa3413)
- Guszejnov, D., Hopkins, P. F., Grudić, M. Y., Krumholz, M. R., & Federrath, C. 2018, *MNRAS*, 480, 182, doi: [10.1093/mnras/sty1847](https://doi.org/10.1093/mnras/sty1847)
- Hanawa, T., & Matsumoto, T. 1999, *ApJ*, 521, 703, doi: [10.1086/307564](https://doi.org/10.1086/307564)
- Hansen, C. E., Klein, R. I., McKee, C. F., & Fisher, R. T. 2012, *ApJ*, 747, 22, doi: [10.1088/0004-637X/747/1/22](https://doi.org/10.1088/0004-637X/747/1/22)
- Haugbølle, T., Padoan, P., & Nordlund, Å. 2018, *ApJ*, 854, 35, doi: [10.3847/1538-4357/aaa432](https://doi.org/10.3847/1538-4357/aaa432)
- Hennebelle, P., & Chabrier, G. 2008, *ApJ*, 684, 395, doi: [10.1086/589916](https://doi.org/10.1086/589916)
- Hennebelle, P., & Grudić, M. Y. 2024, *ARA&A*, 62, 63, doi: [10.1146/annurev-astro-052622-031748](https://doi.org/10.1146/annurev-astro-052622-031748)
- Hopkins, P. F. 2012, *MNRAS*, 423, 2037, doi: [10.1111/j.1365-2966.2012.20731.x](https://doi.org/10.1111/j.1365-2966.2012.20731.x)
- Hunter, C. 1977, *ApJ*, 218, 834, doi: [10.1086/155739](https://doi.org/10.1086/155739)
- Jones, C. E., Basu, S., & Dubinski, J. 2001, *ApJ*, 551, 387, doi: [10.1086/320093](https://doi.org/10.1086/320093)
- Keown, J., Di Francesco, J., Kirk, H., et al. 2017, *ApJ*, 850, 3, doi: [10.3847/1538-4357/aa93ec](https://doi.org/10.3847/1538-4357/aa93ec)
- Kerr, R., Kirk, H., Di Francesco, J., et al. 2019, *ApJ*, 874, 147, doi: [10.3847/1538-4357/ab0c08](https://doi.org/10.3847/1538-4357/ab0c08)
- Kirk, H., Di Francesco, J., Johnstone, D., et al. 2016, *ApJ*, 817, 167, doi: [10.3847/0004-637X/817/2/167](https://doi.org/10.3847/0004-637X/817/2/167)
- Kirk, H., Friesen, R. K., Pineda, J. E., et al. 2017, *ApJ*, 846, 144, doi: [10.3847/1538-4357/aa8631](https://doi.org/10.3847/1538-4357/aa8631)
- Kirk, J. M., Ward-Thompson, D., Palmeirim, P., et al. 2013, *MNRAS*, 432, 1424, doi: [10.1093/mnras/stt561](https://doi.org/10.1093/mnras/stt561)
- Kirk, J. M., Ward-Thompson, D., Di Francesco, J., et al. 2024, *MNRAS*, 532, 4661, doi: [10.1093/mnras/stae1633](https://doi.org/10.1093/mnras/stae1633)
- Klessen, R. S., & Burkert, A. 2000, *ApJS*, 128, 287, doi: [10.1086/313371](https://doi.org/10.1086/313371)
- Könyves, V., André, P., Men'shchikov, A., et al. 2015, *A&A*, 584, A91, doi: [10.1051/0004-6361/201525861](https://doi.org/10.1051/0004-6361/201525861)
- Könyves, V., André, P., Arzoumanian, D., et al. 2020, *A&A*, 635, A34, doi: [10.1051/0004-6361/201834753](https://doi.org/10.1051/0004-6361/201834753)
- Kratter, K., & Lodato, G. 2016, *ARA&A*, 54, 271, doi: [10.1146/annurev-astro-081915-023307](https://doi.org/10.1146/annurev-astro-081915-023307)
- Krumholz, M. R., & McKee, C. F. 2005, *ApJ*, 630, 250, doi: [10.1086/431734](https://doi.org/10.1086/431734)
- Kuiper, R., Turner, N. J., & Yorke, H. W. 2016, *ApJ*, 832, 40, doi: [10.3847/0004-637X/832/1/40](https://doi.org/10.3847/0004-637X/832/1/40)
- Lai, D. 2000, *ApJ*, 540, 946, doi: [10.1086/309361](https://doi.org/10.1086/309361)
- Larson, R. B. 1969, *MNRAS*, 145, 271, doi: [10.1093/mnras/145.3.271](https://doi.org/10.1093/mnras/145.3.271)
- Lee, C. W., Myers, P. C., & Tafalla, M. 1999, *ApJ*, 526, 788, doi: [10.1086/308027](https://doi.org/10.1086/308027)
- . 2001, *ApJS*, 136, 703, doi: [10.1086/322534](https://doi.org/10.1086/322534)
- Lee, K. I., Fernández-López, M., Storm, S., et al. 2014, *ApJ*, 797, 76, doi: [10.1088/0004-637X/797/2/76](https://doi.org/10.1088/0004-637X/797/2/76)
- Lee, Y.-N., & Hennebelle, P. 2018, *A&A*, 611, A89, doi: [10.1051/0004-6361/201731523](https://doi.org/10.1051/0004-6361/201731523)
- Li, P. S., Norman, M. L., Mac Low, M.-M., & Heitsch, F. 2004, *ApJ*, 605, 800, doi: [10.1086/382652](https://doi.org/10.1086/382652)
- Li, S., Sanhueza, P., Zhang, Q., et al. 2023, *ApJ*, 949, 109, doi: [10.3847/1538-4357/acc58f](https://doi.org/10.3847/1538-4357/acc58f)
- Lin, C. C., Mestel, L., & Shu, F. H. 1965, *ApJ*, 142, 1431, doi: [10.1086/148428](https://doi.org/10.1086/148428)
- Lomax, O., Whitworth, A. P., & Cartwright, A. 2013, *MNRAS*, 436, 2680, doi: [10.1093/mnras/stt1764](https://doi.org/10.1093/mnras/stt1764)
- Martel, H., Evans, Neal J., I., & Shapiro, P. R. 2006, *ApJS*, 163, 122, doi: [10.1086/500090](https://doi.org/10.1086/500090)
- McKee, C. F., & Ostriker, E. C. 2007, *ARA&A*, 45, 565, doi: [10.1146/annurev.astro.45.051806.110602](https://doi.org/10.1146/annurev.astro.45.051806.110602)
- McKee, C. F., & Tan, J. C. 2003, *ApJ*, 585, 850, doi: [10.1086/346149](https://doi.org/10.1086/346149)
- McLaughlin, D. E., & Pudritz, R. E. 1997, *ApJ*, 476, 750, doi: [10.1086/303657](https://doi.org/10.1086/303657)
- Moon, S., & Ostriker, E. C. 2024a, *ApJ*, 975, 295, doi: [10.3847/1538-4357/ad7813](https://doi.org/10.3847/1538-4357/ad7813)
- . 2024b, arXiv e-prints, arXiv:2411.07349, <https://arxiv.org/abs/2411.07349>
- Morii, K., Sanhueza, P., Nakamura, F., et al. 2023, *ApJ*, 950, 148, doi: [10.3847/1538-4357/acccca](https://doi.org/10.3847/1538-4357/acccca)

- Motte, F., Bontemps, S., & Louvet, F. 2018, *ARA&A*, 56, 41, doi: [10.1146/annurev-astro-091916-055235](https://doi.org/10.1146/annurev-astro-091916-055235)
- Mowat, C., Hatchell, J., Rumble, D., et al. 2017, *MNRAS*, 467, 812, doi: [10.1093/mnras/stx042](https://doi.org/10.1093/mnras/stx042)
- Myers, P. C., & Fuller, G. A. 1992, *ApJ*, 396, 631, doi: [10.1086/171744](https://doi.org/10.1086/171744)
- Myers, P. C., Fuller, G. A., Goodman, A. A., & Benson, P. J. 1991, *ApJ*, 376, 561, doi: [10.1086/170305](https://doi.org/10.1086/170305)
- Nakamura, F., & Li, Z.-Y. 2008, *ApJ*, 687, 354, doi: [10.1086/591641](https://doi.org/10.1086/591641)
- Neralwar, K. R., Colombo, D., Offner, S., et al. 2024, *A&A*, 690, A345, doi: [10.1051/0004-6361/202451156](https://doi.org/10.1051/0004-6361/202451156)
- Nony, T., Galván-Madrid, R., Motte, F., et al. 2023, *A&A*, 674, A75, doi: [10.1051/0004-6361/202244762](https://doi.org/10.1051/0004-6361/202244762)
- Offner, S. S. R., Clark, P. C., Hennebelle, P., et al. 2014, in *Protostars and Planets VI*, ed. H. Beuther, R. S. Klessen, C. P. Dullemond, & T. Henning, 53–75, doi: [10.2458/azu_uapress.9780816531240-ch003](https://doi.org/10.2458/azu_uapress.9780816531240-ch003)
- Offner, S. S. R., & Krumholz, M. R. 2009, *ApJ*, 693, 914, doi: [10.1088/0004-637X/693/1/914](https://doi.org/10.1088/0004-637X/693/1/914)
- Offner, S. S. R., Moe, M., Kratter, K. M., et al. 2023, in *Astronomical Society of the Pacific Conference Series*, Vol. 534, *Protostars and Planets VII*, ed. S. Inutsuka, Y. Aikawa, T. Muto, K. Tomida, & M. Tamura, 275, doi: [10.48550/arXiv.2203.10066](https://doi.org/10.48550/arXiv.2203.10066)
- Offner, S. S. R., Taylor, J., Markey, C., et al. 2022, *MNRAS*, 517, 885, doi: [10.1093/mnras/stac2734](https://doi.org/10.1093/mnras/stac2734)
- Padoan, P., Federrath, C., Chabrier, G., et al. 2014, in *Protostars and Planets VI*, ed. H. Beuther, R. S. Klessen, C. P. Dullemond, & T. Henning, 77–100, doi: [10.2458/azu_uapress.9780816531240-ch004](https://doi.org/10.2458/azu_uapress.9780816531240-ch004)
- Padoan, P., & Nordlund, Å. 2002, *ApJ*, 576, 870, doi: [10.1086/341790](https://doi.org/10.1086/341790)
- . 2011, *ApJ*, 730, 40, doi: [10.1088/0004-637X/730/1/40](https://doi.org/10.1088/0004-637X/730/1/40)
- Padoan, P., Pan, L., Juvela, M., Haugbølle, T., & Nordlund, Å. 2020, *ApJ*, 900, 82, doi: [10.3847/1538-4357/abaa47](https://doi.org/10.3847/1538-4357/abaa47)
- Pattle, K., Ward-Thompson, D., Kirk, J. M., et al. 2015, *MNRAS*, 450, 1094, doi: [10.1093/mnras/stv376](https://doi.org/10.1093/mnras/stv376)
- . 2017, *MNRAS*, 464, 4255, doi: [10.1093/mnras/stw2648](https://doi.org/10.1093/mnras/stw2648)
- Pattle, K., Bresnahan, D., Ward-Thompson, D., et al. 2025, *MNRAS*, doi: [10.1093/mnras/staf009](https://doi.org/10.1093/mnras/staf009)
- Pelkonen, V. M., Padoan, P., Haugbølle, T., & Nordlund, Å. 2021, *MNRAS*, 504, 1219, doi: [10.1093/mnras/stab844](https://doi.org/10.1093/mnras/stab844)
- Penston, M. V. 1969, *MNRAS*, 144, 425, doi: [10.1093/mnras/144.4.425](https://doi.org/10.1093/mnras/144.4.425)
- Pezzuto, S., Benedettini, M., Di Francesco, J., et al. 2021, *A&A*, 645, A55, doi: [10.1051/0004-6361/201936534](https://doi.org/10.1051/0004-6361/201936534)
- Pineda, J. L., Goldsmith, P. F., Chapman, N., et al. 2010, *ApJ*, 721, 686, doi: [10.1088/0004-637X/721/1/686](https://doi.org/10.1088/0004-637X/721/1/686)
- Redaelli, E., Bovino, S., Sanhueza, P., et al. 2022, *ApJ*, 936, 169, doi: [10.3847/1538-4357/ac85b4](https://doi.org/10.3847/1538-4357/ac85b4)
- Ryden, B. S. 1996, *ApJ*, 471, 822, doi: [10.1086/178010](https://doi.org/10.1086/178010)
- Salji, C. J., Richer, J. S., Buckle, J. V., et al. 2015, *MNRAS*, 449, 1769, doi: [10.1093/mnras/stu2297](https://doi.org/10.1093/mnras/stu2297)
- Sanhueza, P., Contreras, Y., Wu, B., et al. 2019, *ApJ*, 886, 102, doi: [10.3847/1538-4357/ab45e9](https://doi.org/10.3847/1538-4357/ab45e9)
- Simpson, R. J., Johnstone, D., Nutter, D., Ward-Thompson, D., & Whitworth, A. P. 2011, *MNRAS*, 417, 216, doi: [10.1111/j.1365-2966.2011.19163.x](https://doi.org/10.1111/j.1365-2966.2011.19163.x)
- Storm, S., Mundy, L. G., Lee, K. I., et al. 2016, *ApJ*, 830, 127, doi: [10.3847/0004-637X/830/2/127](https://doi.org/10.3847/0004-637X/830/2/127)
- Sugimura, K., Mizuno, Y., Matsumoto, T., & Omukai, K. 2017, *MNRAS*, 469, 4022, doi: [10.1093/mnras/stx1129](https://doi.org/10.1093/mnras/stx1129)
- Tang, M., Liu, T., Qin, S.-L., et al. 2018, *ApJ*, 856, 141, doi: [10.3847/1538-4357/aaadad](https://doi.org/10.3847/1538-4357/aaadad)
- Tassis, K. 2007, *MNRAS*, 379, L50, doi: [10.1111/j.1745-3933.2007.00332.x](https://doi.org/10.1111/j.1745-3933.2007.00332.x)
- Tohline, J. E. 1980a, *ApJ*, 235, 866, doi: [10.1086/157688](https://doi.org/10.1086/157688)
- . 1980b, *ApJ*, 239, 417, doi: [10.1086/158125](https://doi.org/10.1086/158125)
- Verliat, A., Hennebelle, P., González, M., Lee, Y.-N., & Geen, S. 2022, *A&A*, 663, A6, doi: [10.1051/0004-6361/202141765](https://doi.org/10.1051/0004-6361/202141765)
- Ward-Thompson, D., Pattle, K., Kirk, J. M., et al. 2016, *MNRAS*, 463, 1008, doi: [10.1093/mnras/stw1978](https://doi.org/10.1093/mnras/stw1978)
- Yoo, H., Lee, C. W., Chung, E. J., et al. 2023, *ApJ*, 957, 94, doi: [10.3847/1538-4357/acf8c2](https://doi.org/10.3847/1538-4357/acf8c2)

Table 1. Summary of the simulation parameters in selected works

Model	\mathcal{M}_{3D}	$\Delta x/L_{J,0}$	$\Delta m/M_{J,0}$	$M_{\text{char,th}}/M_{J,0}$	$M_{\text{min}}/M_{J,0}$	$M_{\text{min}}/M_{\text{char,th}}$	$\Delta x(\rho_0)/r_{s,\text{cloud}}$
(1)	(2)	(3)	(4)	(5)	(6)	(7)	(8)
M5 (this work)	5	3.9×10^{-3}	-	6.6×10^{-2}	2.4×10^{-2}	0.36	0.043
M10 (this work)	10	3.9×10^{-3}	-	3.3×10^{-2}	2.4×10^{-2}	0.72	0.087
M2e3_R3 (Guszejnov et al. 2020)	9.3	-	5.4×10^{-7}	3.6×10^{-2}	1.2×10^{-3}	0.032	0.17
M2e4_R10 (Guszejnov et al. 2020)	16	-	1.4×10^{-6}	2.1×10^{-2}	3.0×10^{-3}	0.14	0.39
M2e5_R30 (Guszejnov et al. 2020)	29	-	8.5×10^{-6}	1.1×10^{-2}	1.8×10^{-2}	1.6	1.3
high (Haugbølle et al. 2018)	10	3.4×10^{-4}	-	3.3×10^{-2}	2.1×10^{-3}	0.063	0.35
M8L2N512 (Gong & Ostriker 2015)	-	2.0×10^{-3}	-	8.6×10^{-2}	1.2×10^{-2}	0.14	-

NOTE—Columns (3) and (4) provide the highest resolution (i.e., smallest Δx for Eulerian simulations and smallest Δm for Lagrangian simulations) of the models used for convergence study given in Column (1). All simulations are inherently scale-free and the choice of $L_{J,0}$ and $M_{J,0}$ is arbitrary. Because Guszejnov et al. (2020) and Haugbølle et al. (2018) present their results in physical units, we provide their adopted values for convenience: $L_{J,0} = 1.3$ pc, $M_{J,0} = 37 M_\odot$ (M2e3_R3); $L_{J,0} = 2.4$ pc, $M_{J,0} = 71 M_\odot$ (M2e4_R10); $L_{J,0} = 4.0$ pc, $M_{J,0} = 120 M_\odot$ (M2e5_R30); $L_{J,0} = 0.71$ pc, $M_{J,0} = 17 M_\odot$ (high). Because the inflow Mach numbers in Gong & Ostriker (2015) cannot be directly related to \mathcal{M}_{3D} , we use the directly measured post-shock density to calculate $M_{\text{char,th}}$ rather than from Equation (34) (see text). For the same reason, it is not straightforward to infer $r_{s,\text{cloud}}$ in their simulations; we thus leave it out in this table.

APPENDIX

A. NUMERICAL RESOLUTION IN GRAVO-TURBULENT SIMULATIONS

To cross-compare the numerical resolutions of different simulations that have been used to address the question of numerical convergence of mass functions, Table 1 lists resolution parameters in some recent simulations, including this work. Column (1) gives the model name and reference. Column (2) gives the cloud-scale Mach number. Columns (3) and (4) give the numerical resolution Δx and Δm for fixed spatial- and fixed mass-resolution simulations, respectively, normalized by the Jeans scales at the mean cloud condition (for the adaptive mesh refinement (AMR) simulations, we indicate Δx at the highest refinement level). Column (5) gives the characteristic mass $M_{\text{char,th}}$ from Equation (34). Column (6) gives the minimum resolvable mass M_{min} from Equations (26) and (27), adopting $N_{\text{core,res}} = 8$ and using either Δx or Δm given in Columns (3)–(4). Column (7) gives the ratio $M_{\text{min}}/M_{\text{char,th}}$. Column (8) gives the numerical resolution at the mean density divided by the sonic scale, where we take the effective spatial resolution $\Delta x(\rho_0) = (\Delta m/\rho_0)^{1/3}$ for fixed mass-resolution simulations.

If the core mass function peaks roughly around $M_{\text{char,th}}$ predicted by various theories, clearly resolving the peak in numerical simulations would require $M_{\text{min}}/M_{\text{char,th}} \ll 1$. Combining Equations (26), (27) and (34), one can show that

$$\frac{M_{\text{min}}}{M_{\text{char,th}}} = 2.32 \mathcal{M}_{3D} N_{\text{core,res}} \left(\frac{\Delta x}{L_{J,0}} \right) \quad (\text{A1a})$$

$$= 12.5 \mathcal{M}_{3D} N_{\text{core,res}}^3 \left(\frac{\Delta m}{M_{J,0}} \right). \quad (\text{A1b})$$

This ratio is linearly proportional to the resolution (either Δx or Δm normalized to the Jeans scales at mean density), and is also linear in the Mach number, making it more difficult to resolve the peak of the CMF in higher Mach number simulations. Although Table 1 is far from being complete, Equation (A1) suggests that simulations should typically find the peak of the CMF (and possibly the SMF, modulo disk fragmentation) converges provided that $M_{\text{min}}/M_{\text{char,th}}$ is sufficiently small. For our lower Mach number simulations, the ratio $M_{\text{min}}/M_{\text{char,th}} = 0.36$, while for our higher Mach number simulations this ratio is 0.72. Thus, we expect to identify the CMF peak clearly in our M5 model but not in our M10, and indeed this appears consistent with our results.

The model [Guszejnov et al. \(2020\)](#) used for their SMF numerical convergence study (M2e5_R30) has a fairly high Mach number $\mathcal{M}_{3D} = 29$, such that $M_{\min}/M_{\text{char,th}} = 1.6$ at their highest mass resolution (i.e., smallest $\Delta m = 10^{-3} M_{\odot} = 8.5 \times 10^{-6} M_{J,0}$). Thus, this set of numerical parameters would not be suitable for identifying the peak of CMF. However, the lower Mach number models in [Guszejnov et al. \(2020\)](#) (M2e3_R3 and M2e4_R10) have ratio $M_{\min}/M_{\text{char,th}} = 0.032\text{--}0.14$, making them suitable to resolve a CMF peak. Indeed, their rerun of model M2e4_R10, after the error in the sink particle algorithm was corrected ([Guszejnov et al. 2021](#)), shows a peak in the SMF near $M_{\text{char,th}} = 2.1 \times 10^{-2} M_{J,0} = 1.5 M_{\odot}$ (conversion to physical units adopting their sound speed and mean density).

In the AMR simulations of a $\mathcal{M}_{3D} = 10$ cloud conducted by [Haugbølle et al. \(2018\)](#), the minimum resolvable mass at their highest refinement level ($\Delta x = 50 \text{ au} = 3.4 \times 10^{-4} L_{J,0}$ adopting their mean cloud density and sound speed) is $M_{\min} = 2.1 \times 10^{-3} M_{J,0} (N_{\text{core,res}}/8)$ from [Equation \(26\)](#). This leads to $M_{\min}/M_{\text{char,th}} = 0.063$ if we adopt $N_{\text{core,res}} = 8$. [Pelkonen et al. \(2021\)](#) performed convergence analysis using the same simulation data of [Haugbølle et al. \(2018\)](#), finding that the SMF in their simulation converges to $0.17 M_{\odot}$ with increasing numerical resolution. They also found that the corresponding progenitor core mass is $0.26 M_{\odot} = 1.5 \times 10^{-2} M_{J,0}$, which is a factor of 2.2 lower than $M_{\text{char,th}}$. We note that the CCMF in our model M5 also suggests a peak at a factor of ~ 2 lower than $M_{\text{char,th}}$ ([Figure 6\(a\)](#)), similar to the results of [Pelkonen et al. \(2021\)](#).

[Gong & Ostriker \(2015\)](#) performed local simulations focusing on a small portion of a GMC where the flows are supersonically converging, using an idealized converging flow setup. Due to the instability in the non-magnetized post-shock layer, their measured average density within the post-shock layer is only weakly dependent on the *inflow* Mach number such that [Equation \(34\)](#) is not straightforwardly applicable. Instead, we use their measured average post-shock density $\rho_{\text{ps}} \sim 15\rho_0$ to estimate the characteristic mass $M_{\text{char,th}} = M_{\text{BE}}(\bar{\rho} = \rho_{\text{ps}}) = 8.6 \times 10^{-2} M_{J,0}$. The minimum resolvable mass at their highest resolution model with $\Delta x = 2 \times 10^{-3} L_{J,0}$ is $M_{\min} = 1.2 \times 10^{-2} M_{J,0} (N_{\text{core,res}}/8)$, a factor of 7 lower than $M_{\text{char,th}}$ for $N_{\text{core,res}} = 8$. They found that the peak of the CMF is numerically converged (see their [Figure 9](#)), with the measured peak location consistent with $M_{\text{char,th}}$. It is worth noting that [Gong & Ostriker \(2015\)](#) used the CMF constructed from the core masses measured at the end of collapse (t_{coll}) for individual core.

Although we choose the resolution of our simulations carefully to resolve most of the core formation *by mass* (see [Section 3.3 of Paper II](#)), resolving the peak of the CMF poses a severe challenge because the mass fraction below the peak is very small. For example, if we assume the peak of the CMF occurs at $M_{\text{peak}} \sim 0.5 M_{\text{char,th}}$ as it appears to be the case in this work and in [Pelkonen et al. \(2021\)](#), clear identification of the peak would require at least $M_{\min} < (1/2) M_{\text{peak}} = 0.25 M_{\text{char,th}}$. [Equation \(A1\)](#) then leads to the following resolution requirement for simulations with a fixed spatial resolution:

$$\frac{\Delta x}{L_{J,0}} < 1.35 \times 10^{-3} \left(\frac{N_{\text{core,res}}}{8} \right)^{-1} \left(\frac{\mathcal{M}_{3D}}{10} \right)^{-1}, \quad (\text{A2})$$

and the requirement for fixed mass resolution:

$$\frac{\Delta m}{M_{J,0}} < 3.91 \times 10^{-6} \left(\frac{N_{\text{core,res}}}{8} \right)^{-3} \left(\frac{\mathcal{M}_{3D}}{10} \right)^{-1}. \quad (\text{A3})$$

Considering that the size of the computational domain should be properly scaled with \mathcal{M}_{3D} to keep the cloud scale virial parameter constant, the total number of simulation elements for a uniform mesh would be

$$\begin{aligned} N^3 &= \left(\frac{L_{\text{box}}}{\Delta x} \right)^3 \\ &= (2698)^3 \left(\frac{N_{\text{core,res}}}{8} \right)^3 \left(\frac{\alpha_{\text{vir,box}}}{2} \right)^{-3/2} \left(\frac{\mathcal{M}_{3D}}{10} \right)^6, \end{aligned} \quad (\text{A4})$$

where we used [Equation \(20\)](#). Similarly, the required number of resolution elements for the fixed mass-resolution simulations is

$$\begin{aligned} N_p &\equiv \frac{M_{\text{box}}}{\Delta m} \\ &= 1.24 \times 10^7 \left(\frac{N_{\text{core,res}}}{8} \right)^3 \left(\frac{\alpha_{\text{vir,box}}}{2} \right)^{-3/2} \left(\frac{\mathcal{M}_{3D}}{10} \right)^4. \end{aligned} \quad (\text{A5})$$

We note that [Equations \(A4\) and \(A5\)](#) are minimum requirements and that even higher resolutions would be required to robustly demonstrate the numerical convergence of the identified peak.

Taken at face value, [Equations \(A4\) and \(A5\)](#) suggest that it might be easier to resolve the peak of the CMF by adopting a fixed mass-resolution rather than fixed spatial resolution. However, it is worth emphasizing that in addition to [Equation \(A2\)](#) for resolving cores, the effective spatial resolution in low-density regions must also be sufficiently high to resolve the sonic scale of turbulence. Column (8) of [Table 1](#) shows that, compared to other current simulations with adaptive resolution, the uniform resolution adopted in this work allows smaller $\Delta x(\rho_0)/r_{s,\text{cloud}}$ and thus better resolves early nonlinear structures created by turbulence.

More generally, [Paper II](#) (see Equation (51) there) shows that resolving $r_{s,\text{cloud}}$ imposes a resolution requirement that has the same Mach number scaling as [Equation \(A4\)](#). However, [Paper II](#) (see Section 5.2 there) also demonstrated that the local sonic scale exhibits an order of magnitude variations (which is correlated with density) above and below $r_{s,\text{cloud}}$, which then demands higher resolution in moderate-density gas. To meet this additional requirement at mean cloud density, i.e., $\Delta x(\rho_0) \ll r_{s,\text{cloud}}$, simulations adopting a fixed mass resolution need to satisfy not only [Equation \(A5\)](#) but also additionally

$$N_p = \frac{M_{\text{box}}}{\Delta m} = 1.90 \times 10^{10} \left(\frac{N_{s,\text{res}}}{30} \right)^3 \left(\frac{\mathcal{M}_{3\text{D}}}{10} \right)^6, \quad (\text{A6})$$

where $N_{s,\text{res}} = r_{s,\text{cloud}}/\Delta x(\rho_0) = 30$ is recommended in [Paper II](#).⁷ Thus, properly resolving the sonic scale is in fact more computationally challenging than resolving self-gravitating cores, whether for fixed mesh or moving mesh simulations.

⁷ In [Paper II](#), we defined $N_{s,\text{res}}$ with respect to sonic scale $\lambda_{s,\text{cloud}} = (4/3)r_{s,\text{cloud}}$ and recommended $\lambda_{s,\text{cloud}}/\Delta x = 40$, which is equivalent to $N_{s,\text{res}} = 30$ presented here.